



# Aftershock patterns of the 2021 $M_w$ 6.3 Northern Thessaly (Greece) earthquake

Georgios Michas · Kyriaki Pavlou ·  
Sophia-Ekaterini Avgerinou ·  
Eleni-Apostolia Anyfadi · Filippos Vallianatos

Received: 5 August 2021 / Accepted: 15 December 2021 / Published online: 25 January 2022  
© The Author(s), under exclusive licence to Springer Nature B.V. 2022

**Abstract** On March 3, 2021, a strong shallow earthquake of magnitude  $M_w$  6.3 struck Northern Thessaly, an area that lies in one of the most active fault zones of mainland Greece. The mainshock generated numerous aftershocks, with some of large magnitude reaching up to  $M_w$  6.0. In this work, we study the scaling properties and the physical mechanisms of aftershock occurrence during the pronounced aftershock sequence that followed the mainshock. The aftershock sequence obeys well-established scaling relationships, such as the Gutenberg-Richter scaling law for the frequency-magnitude distribution of aftershocks with a  $b$ -value of

$0.90 \pm 0.03$  and a composite model of three modified Omori regimes for the decay of the aftershocks production rate. The distribution of waiting times between the successive aftershocks also presents scaling and a bimodal distribution between two power-law regimes, signifying clustering effects at all time scales in the temporal occurrence of aftershocks. Application of principal component analysis to the spatial distribution of aftershocks indicates that the activated area reached its maximum during the first ten days after the mainshock and then remained constant. Aftershocks mainly propagated along fault strike on a NW–SE direction during the early phase of postseismic relaxation, driven by a combination of co-seismic stress changes and afterslip following the mainshock. Overall, the results presented herein provide important insights into the scaling parameters and the triggering mechanisms of the 2021 Northern Thessaly aftershock sequence, which are essential for better understanding and modeling the aftershock generation process.

## Article highlights

- A strong earthquake of magnitude 6.3 struck northern Thessaly on March 2021, producing numerous aftershocks.
- The aftershock sequence presents scaling in the distributions of earthquake magnitudes and temporal occurrence.
- Aftershocks migrated along fault strike as the combined effect of co-seismic stress changes and afterslip.

G. Michas (✉) · K. Pavlou · S.-E. Avgerinou · E.-A. Anyfadi · F. Vallianatos  
Section of Geophysics – Geothermics, Department of Geology and Geoenvironment, National and Kapodistrian University of Athens, Athens, Greece  
e-mail: gemichas@geol.uoa.gr

G. Michas · S.-E. Avgerinou · E.-A. Anyfadi ·  
F. Vallianatos  
Institute of Physics of Earth's Interior and Geohazards,  
UNESCO Chair On Solid Earth Physics and Geohazards  
Risk Reduction, Hellenic Mediterranean University  
Research Center, Crete, Greece

**Keywords** 2021 Northern Thessaly earthquake · Aftershock sequence · Scaling properties · Triggering mechanisms · Coulomb stress transfer · Afterslip

## 1 Introduction

The occurrence of pronounced aftershock sequences following large earthquakes is one of the most well-established patterns of observational seismology.

Aftershock generation can be attributed to the relaxation process of stress concentrations produced by the dynamic rupture of the mainshock (e.g., Scholz 2019). To explain the occurrence of aftershocks, various physical mechanisms have been proposed, including rate and state-dependent friction (Dieterich 1994), viscoelastic relaxation (Dieterich 1972; Nakanishi 1992), stress corrosion evolving in sub-critical crack growth (Das and Scholz 1981), pore fluid flow (Nur and Booker 1972; Miller et al. 2004), fault damage rheology (Shcherbakov and Turcotte 2004; Ben-Zion and Lyakhovsky 2006), and aseismic slip (Perfettini and Avouac 2004; Hsu et al. 2006), among others. The main objective of these mechanisms is to provide a physical reasoning to certain aspects that are manifested in the statistical properties of aftershock sequences. Perhaps the most robust one is the frequency-magnitude distribution of aftershocks that, as all earthquakes, scale according to the Gutenberg-Richter scaling law (Gutenberg and Richter 1944). The other well-established scaling relationship refers to the decay of the aftershock production rate that scales as a power-law with time according to the modified Omori formula (Utsu et al. 1995). In addition, the spatial distribution of aftershocks frequently presents migration patterns with time, albeit not universally observed (Tajima and Kanamori 1985; Henry and Das 2001; Helmstetter et al. 2003). All these properties can provide important insights into the spatiotemporal organization, the internal dynamics, and overall, into the physical mechanisms of aftershocks occurrence.

On March 3, 2021, a strong shallow earthquake of moment magnitude  $M_w$  6.3 occurred in Northern Thessaly (central Greece), with seismic intensity reaching in the epicentral area the magnitude VIII of the modified Mercalli scale (USGS NEIC ShakeMap, available at <https://earthquake.usgs.gov/>). The earthquake has widely been felt in central Greece and has caused one casualty, few injuries, and severe building damages in the broader epicentral area (e.g., Mavroulis et al. 2021). The  $M_w$  6.3 mainshock was followed by numerous aftershocks, with some reaching or exceeding  $M_w$  5.0. One day later, on March 4, 2021, a second major event with magnitude  $M_w$  6.0 occurred to the northwest of the mainshock. Aftershock productivity was intense during the first 2 weeks after the mainshock counting a few thousand of events and then slowed down. The aftershock activity progressed

along a NW–SE general direction, consistent with the focal mechanisms of the mainshock and the major events, as well as with the regional tectonic setting (Ganas et al. 2021; Karakostas et al. 2021).

In this study, we provide the first results regarding the scaling properties and the spatial distribution of the 2021 Northern Thessaly aftershock sequence and investigate the triggering mechanisms. Initially, we consider aftershocks as a point-process in time and space, marked by the magnitude of the event, and estimate the parameters of well-established empirical scaling relationships for aftershock sequences, such as the Gutenberg-Richter scaling law for the frequency-magnitude distribution of earthquakes and the modified-Omori formula for the aftershocks decay rate. To provide further insights into the physical mechanism of the aftershock generation process, we also investigate the distribution of waiting times between successive events. In addition, we investigate the spatial distribution of aftershocks and its correlation to positive Coulomb stress changes induced by the mainshock and the second major event. We further study the rate of the spatial expansion of the aftershocks focal zone by using principal component analysis and discuss the results in terms of rate strengthening rheology that governs the evolution of the afterslip process.

## 2 Regional seismotectonic setting and the 2021 $M_w$ 6.3 earthquake

Thessaly region belongs to the western margin of Internal Hellenides in the back-arc of the Aegean microplate. The geology of the broader epicentral area consists mainly of metamorphic formations covered by carbonate rocks that belong to the Pelagonian unit. The metamorphic rocks include formations of marbles and crystallized limestones, as well as blueschists, gneisses, schists, and amphibolites (Paleozoic – Triassic age) (Fig. 1) (Caputo 1990). Other Mesozoic formations as granites and granodiorites are observed to the north of the epicentral area, as well as small-scale appearances of ophiolites (Fig. 1). Post-alpine sediments as molassic formations are observed to the west, while Quaternary deposits spread towards the east and south (Fig. 1) (Caputo and Pavlides 1993).

Northern Thessaly experiences active continental extension of the order of 2–4 mm/year on an N–S

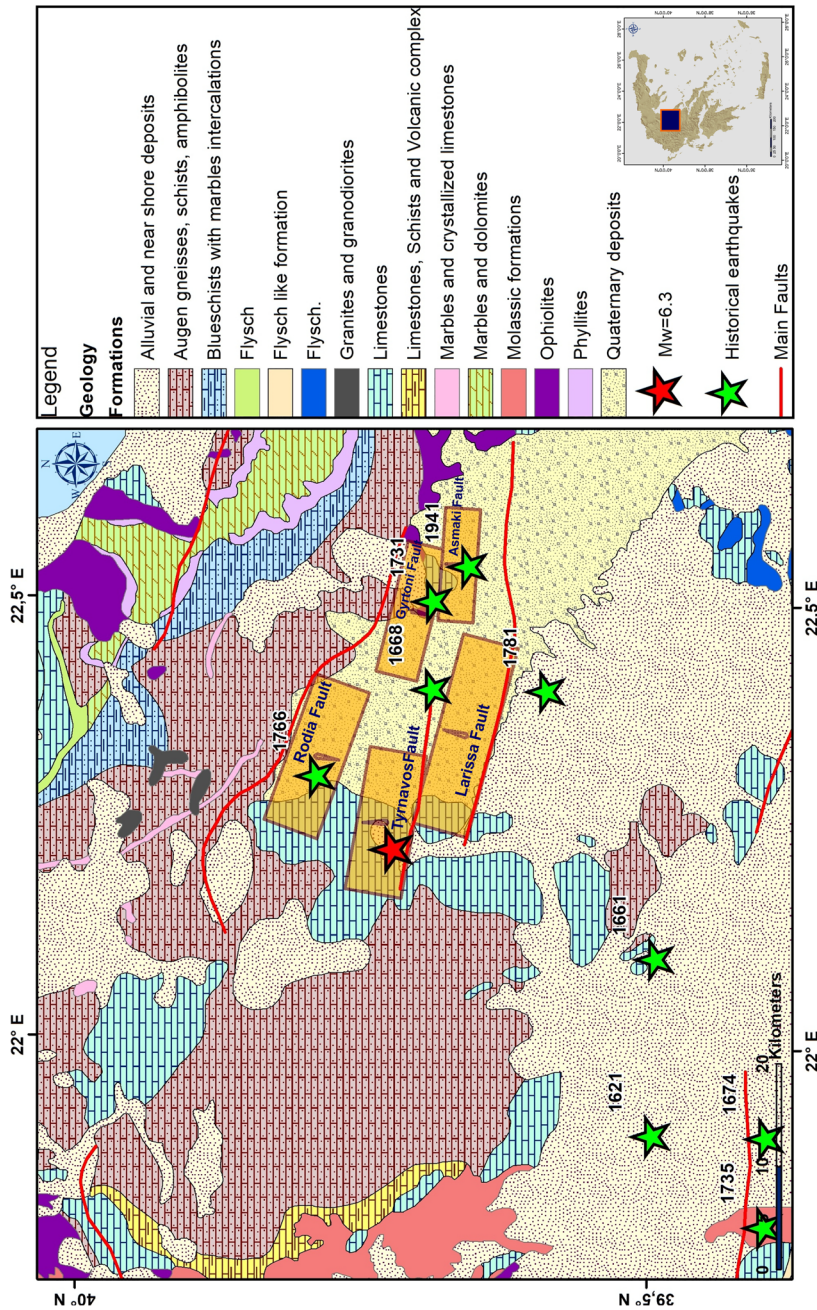


**Fig. 1** Simplified geological map of Northern Thessaly, based on the map of IGME (Bor novas and Rongodianni-Tsiambaou 1983). The red star marks the epicenter of the 2021  $M_w$  6.3 earthquake, while green stars the epicenters of regional historic earthquakes (Papazachos and Papazachou 2003). Solid lines and rectangles show the regional mapped faults according to GREDASS 2.0 (Caputo and Pavlides 2013); TF, Tyrnavos Fault; LF, Larissa Fault; RF, Rodia Fault; GF, Gyrtomi Fault; AF, Asmaki Fault

to NNE–SSW direction (D’Agostino et al. 2020). NE–SW extension during Late Miocene–Early Pleistocene was succeeded in Middle Pleistocene by a new deformation phase of roughly N–S extension that is still active. This deformation phase formed a new system of E–W to ESE–WNW trending normal faults and the Tyrnavos Basin (Caputo et al. 2004), in which the epicenter of the 2021  $M_w$  6.3 earthquake is located. The Tyrnavos Basin is bordered by few major normal faults, as the south-dipping Rodia and Gyroni faults to the north and the north-dipping Tyrnavos, Larissa, and Asmaki faults to the south (Caputo et al. 2004) (Fig. 1).

Thessaly area is located on the western termination of the North Anatolian Fault zone (Hatzfeld et al. 1999; Müller et al. 2013) and is characterized by high seismicity, with numerous earthquakes reported in both historic and modern times. Regional large earthquakes present typical mainshock magnitudes between 6.0 and 7.0. During 1500–1900 CE, thirteen earthquakes with  $M \geq 6.0$  are reported in the region of Thessaly (Table 1), three of which were in the vicinity of Larissa (1668,  $M$  6.0; 1731,  $M$  6.0; 1781,  $M$  6.2) and one (1766,  $M$  6.1) close to Ellassona (Papazachos and Papazachou 2003; Stucchi et al. 2013) (Fig. 1). During the twentieth century, six large earthquakes with  $M \geq 6.0$  have occurred in this area (Table 1), with the 1954,  $M$  7.0 Sofades earthquake being the most destructive one, causing severe building damages in the broader Southern Thessaly region (Papazachos and Papazachou 2003; Papadimitriou and Karakostas 2003). The 1941  $M$  6.3 Larissa, the 1957  $M$  6.8 Velestino, and the 1980  $M$  6.5 Almyros earthquakes are equally notable events, with similarly destructive consequences (Papazachos et al. 1983; Caputo and Pavlides 1993; Papazachos and Papazachou 2003; Papadimitriou and Karakostas 2003). During the last five centuries, strong earthquakes in this area seem to be clustered in time and space, implying interactions between the regional active faults (Papadimitriou and Karakostas 2003).

On February 28, 2021, seismicity started to increase in the Tyrnavos basin, registering few shallow earthquakes with magnitude  $M \leq 2.7$  and depth  $D < 10$  km. Three days later, on March 3, 2021 (time 10:16:08 UTC), the  $M_w$  6.3 strong earthquake occurred in the area, at a depth of  $\sim 10$  km (Karakostas et al. 2021) and at a distance of  $\sim 8$  km W of Tyrnavos,  $\sim 23$  km WNW of Larissa and  $\sim 43$  km

**Table 1** Reported earthquakes with  $M \geq 6.0$  in the region of Thessaly during 1500–2020

Year	Latitude	Longitude	Magnitude	Area
1544	39.50	21.60	6.4	Pyli
1621	39.50	21.90	6.0	Meteora
1661	39.50	22.10	6.2	Meteora
1665	39.60	21.60	6.0	Pyli
1668	39.70	22.40	6.0	Larissa
1674	39.40	21.90	6.0	Meteora
1731	39.70	22.50	6.0	Larissa
1735	39.40	21.80	6.4	Meteora
1743	39.40	22.60	6.6	Almyros
1766	39.80	22.30	6.1	Ellassona
1773	39.40	22.70	6.4	Almyros
1781	39.60	22.40	6.2	Larissa
1787	39.60	21.40	6.0	Pyli
1905	39.67	22.93	6.4	Skiti
1941	39.67	22.54	6.3	Larissa
1954	39.28	22.29	7.0	Sofades
1957	39.30	22.70	6.5	Velestino
1957	39.38	22.63	6.8	Velestino
1980	39.27	22.93	6.5	Almyros

ENE of Trikala. The moment tensor solution of the mainshock indicates the activation of a NW–SE normal fault, dipping towards SW or NE (Fig. 2), while the hypocentral distribution of aftershocks points to a NE-dipping intermediate-angle fault plane (Ganas et al. 2021). The mainshock was instantly followed by numerous aftershocks, with some reaching or exceeding  $M_w$  5.0, while one day later, on March 4, 2021 (time 18:38:18 UTC), the  $M_w$  6.0 second major event occurred to the northwest of the mainshock (Fig. 2). The focal mechanism of the  $M_w$  6.0 earthquake, as well as the ones of the largest aftershocks, indicate normal faulting in a NW–SE general direction, alike the focal mechanism of the mainshock (Fig. 2). The depth range of the aftershock sequence was mainly between  $\sim 4$  and  $\sim 12$  km (Karakostas et al. 2021). The two  $M_w \geq 6$  major events, as well as the March 12, 2021,  $M_w$  5.5 aftershock, are thought to have ruptured three previously unknown blind normal faults (Ganas et al. 2021).

The spatial distribution of the aftershock sequence during the period March 3–May 21, 2021, as extracted from the bulletins of the Geophysics Department, Aristotle University of Thessaloniki

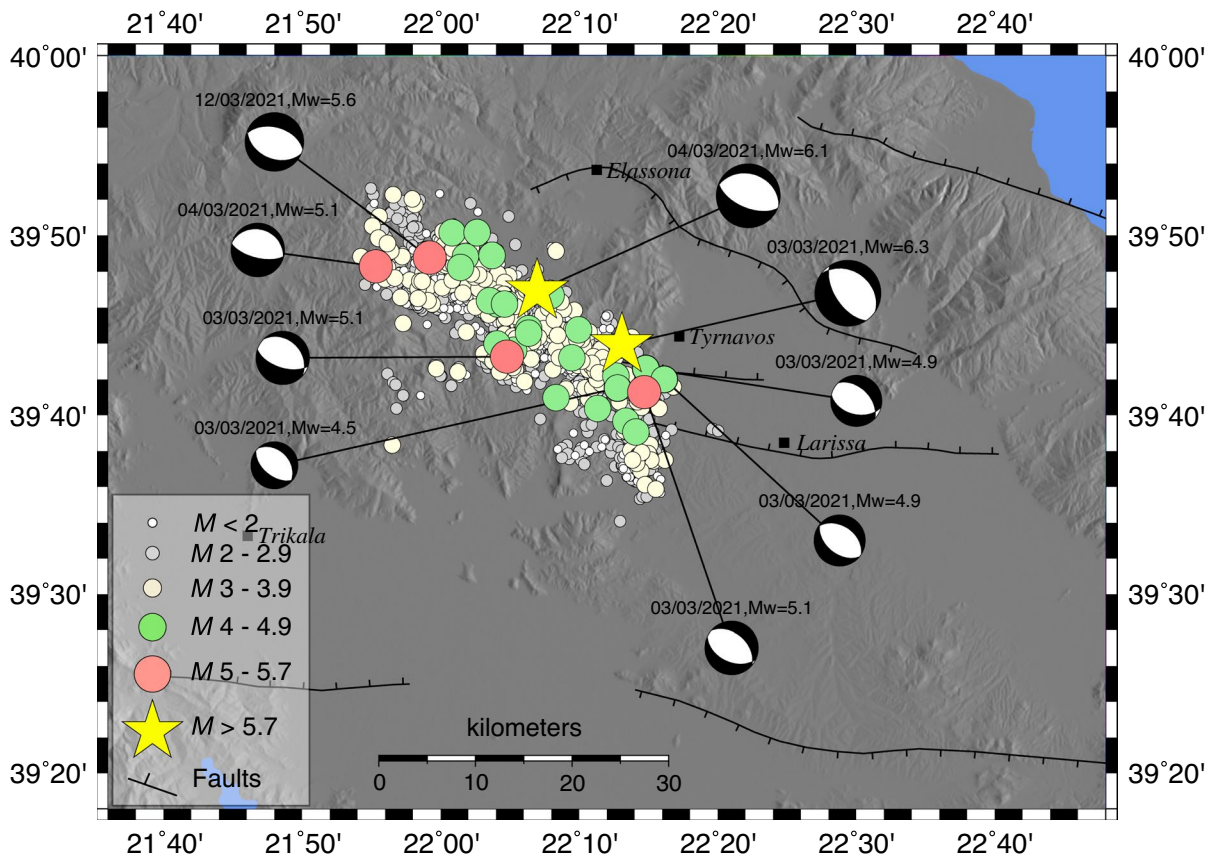


**Fig. 2** The spatial distribution of the 2021 Northern Thessaly aftershock sequence (filled symbols, scaled according to magnitude). Beachballs represent the focal mechanisms of the

larger earthquakes, according to the moment tensor solutions of the Institute of Geodynamics, National Observatory of Athens (<http://bbnet.gein.noa.gr/>)

(AUTH) (<http://geophysics.geo.auth.gr/ss/>), counting 1867 events, is shown in Fig. 2. Aftershocks align towards NW–SE, in agreement with the general direction of the regional tectonic setting (Fig. 1) and the strike of the major events (Fig. 2). The aftershock hypocenters are located at crustal depths, mainly shallower than ~10 km. However, as depths are less well constrained in the AUTH bulletins, they are not depicted in Fig. 2. The rate of earthquake magnitudes during this period is shown in Fig. 3 according to the AUTH bulletins. In the latter, earthquake magnitudes are registered at the local scale, referring to magnitude  $M$  6.0 and  $M$  5.8 for the mainshock and the second major event, respectively (Fig. 3; stars). In Fig. 3, it can also be observed the augmentation of the recorded lower magnitude events, after the installation of a local network on March 5, 2021, by AUTH. Throughout the analysis, we refer to local magnitudes

( $M$ ) as registered in the AUTH bulletins, unless otherwise we refer in the text to the revised moment magnitudes ( $M_w$ ) of the larger events.

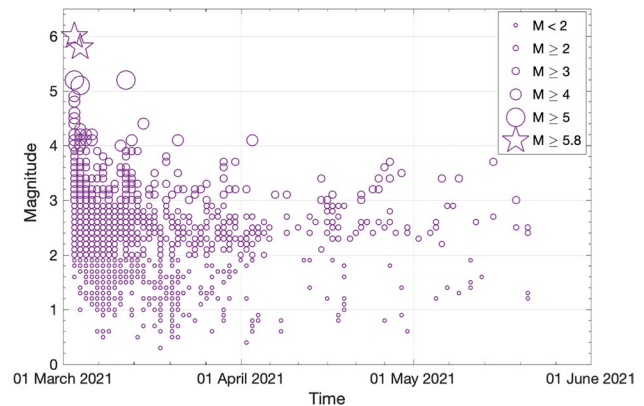
### 3 Scaling properties of the aftershock sequence

#### 3.1 Frequency-size distribution and seismic b-values

The frequency-magnitude distribution of earthquakes and aftershock sequences, under a wide variety of conditions and scales, is well approximated with the Gutenberg–Richter (G-R) scaling law (Gutenberg and Richter 1944):

$$\log N(> M) = a - bM \tag{1}$$

**Fig. 3** The rate of earthquake magnitudes (local scale) with time for the 2021 Northern Thessaly aftershock sequence during the period March 03–May 21, 2021, according to the AUTH bulletins



where  $N(>M)$  is the number of earthquakes with magnitude greater than  $M$  and  $a$ ,  $b$  are positive constants that represent the regional level of seismicity and the proportion of small to larger magnitude events, respectively. The parameter  $b$ , commonly known as the seismic  $b$ -value, generally takes values close to one (Frohlich and Davis 1993; Scholz 2019), although regional variations may appear that can be attributed to the regional stress regime (Schorlemmer et al. 2005). Various studies have shown that aftershocks also satisfy the G-R relation, with  $b$ -values that are generally not different from those of regional or background seismicity (e.g., Kisslinger 1996).

To calculate the  $a$  and  $b$  parameters of Eq. 1, the maximum likelihood estimation (MLE) procedure is commonly deployed (Utsu 1966; Shi and Bolt 1982). In these calculations, it is crucial to appropriately define  $M_0$ , the minimum earthquake magnitude that is considered in the analysis; otherwise, biases can be produced in the estimated values. To appropriately define  $M_0$ , we estimate the magnitude of completeness ( $M_c$ ) of the seismic dataset during the period March 3–May 21, 2021, according to two methods, the maximum curvature method and the goodness-of-fit test (Wiemer and Wyss 2000). The maximum curvature method provides  $M_c=2.3$ . The goodness-of-fit test provides a similar value ( $M_c=2.3$ ) for 90% residuals, while for 95% residuals, it provides  $M_c=2.4$  (Fig. 4a). In the following we consider the more conservative value of  $M_c=2.4$  and use in the statistical analysis only the events with  $M \geq M_c$ , counting 974 events.

Setting  $M_0=2.4$ , we calculate the  $a$  and  $b$  values of the G-R relation using the MLE method. For the 2021 Northern Thessaly aftershock sequence, we estimate

the values of  $a=5.13 \pm 0.11$  and  $b=0.90 \pm 0.03$ . Figure 4c shows the frequency–magnitude distribution for the aftershock sequence and the fitting according to the G-R scaling law (Eq. 1) for the estimated model parameters. The fitting is generally well constrained, suggesting that the G-R scaling law is applicable in this sequence with  $b=0.90$ . Furthermore, we calculated the corresponding  $a$  and  $b$  values for the regional background seismic activity enclosed within the area of Fig. 1 during 2011–2020. In this case, we used the bulletins of the Hellenic Unified Seismological Network (HUSN) (<http://bbnet.gein.noa.gr/HL/>) that counts 514 events during this period. Using the previous methodology, we estimated the magnitude of completeness  $M_c=2.0$  for 95% residuals (Fig. 4b). Setting  $M_0=2.0$ , the  $a$  and  $b$  values of the G-R relation are  $a=4.50 \pm 0.18$  and  $b=1.10 \pm 0.07$  (Fig. 4d). Hence, we observe that the regional background  $b$ -value during 2011–2020 is higher than the  $b$ -value of the aftershock sequence, or the value of  $b=0.96$  that characterizes the longer-term seismic activity in the area of Northern Thessaly (Vamvakaris et al. 2016), mainly due to the lack of larger magnitude earthquakes during the last decade prior to the 2021 mainshock.

In addition, we calculated the  $b$ -value variations during the aftershock sequence. Initially, we estimated the magnitude of completeness ( $M_c$ ) in consecutive time windows comprising of 200 events sliding every 50 events. As the goodness-of-fit test did not always provide a result for 95% residuals in the successive time windows, we considered the results for  $M_c$  calculated with the maximum curvature method. The variations of  $M_c$  with time are shown in Fig. 5a.  $M_c$  varies between 2.2 and 2.4

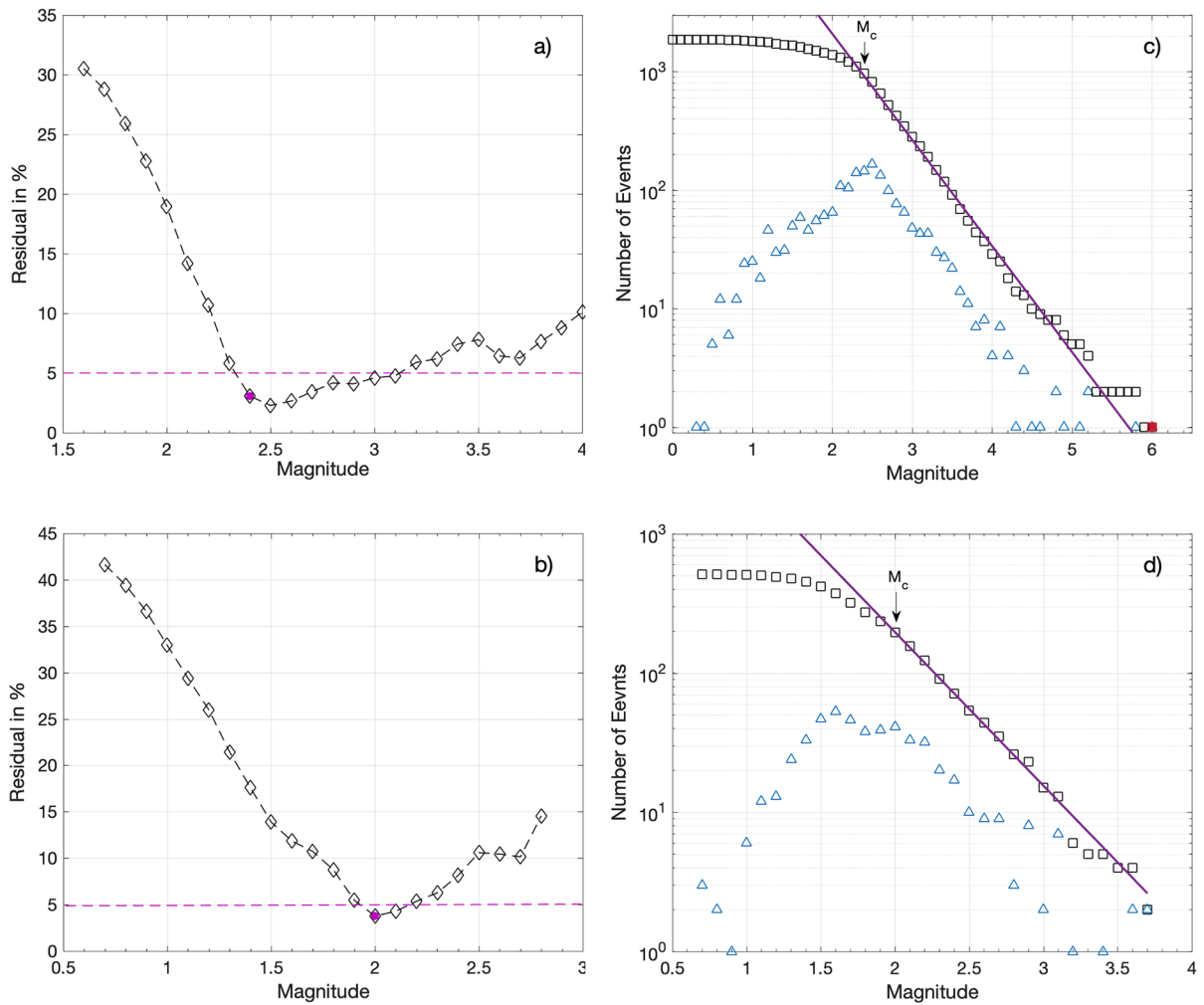


**Fig. 4** **a** Residual plot between the observed frequency–magnitude distribution and the perfect fit of a power-law for each magnitude bin for the 2021 Northern Thessaly aftershock sequence. The purple dot indicates  $M_c$  for 95% residuals. **b** The same plot for the 2011–2020 seismic activity in Northern Thessaly. **c** Frequency–magnitude distribution of the 2021 Northern Thessaly aftershock sequence, represented by the

cumulative (squares) and the discrete (triangles) number of events. The solid line represents the G-R relation for  $M_c=2.4$  and for the values of  $a=5.13$  and  $b=0.90$ . **d** The same plot as previously, for the 2011–2020 seismic activity in Northern Thessaly. The solid line represents the G-R relation for  $M_c=2.0$  and for the values of  $a=4.50$  and  $b=1.10$

during the first 4 days after the mainshock, while it drops down to 2.0 on March 8, 2021, following the installation of the local network on March 5. From thereon,  $M_c$  varies between 2.1 and 2.4 (Fig. 5a). We then calculated the  $b$ -value of the G-R relation and its uncertainties using the same methodology as previously and setting  $M_0$  equal to  $M_c$  for each time window. The results, shown in Fig. 5b, indicate variations between  $0.62 \pm 0.04$  and  $1.10 \pm 0.10$ ,

with a mean of  $0.92 \pm 0.08$ . The lowest value of  $b=0.62 \pm 0.04$  appears right after the mainshock occurrence, probably due to incompleteness of the catalogue in the lower magnitude earthquakes during the first hours after the mainshock (e.g., Kagan 2004). Then the  $b$ -value increased during the following days, reaching the value of  $1.10 \pm 0.10$  during March 9, and then dropped and varied around the mean value (Fig. 5b).

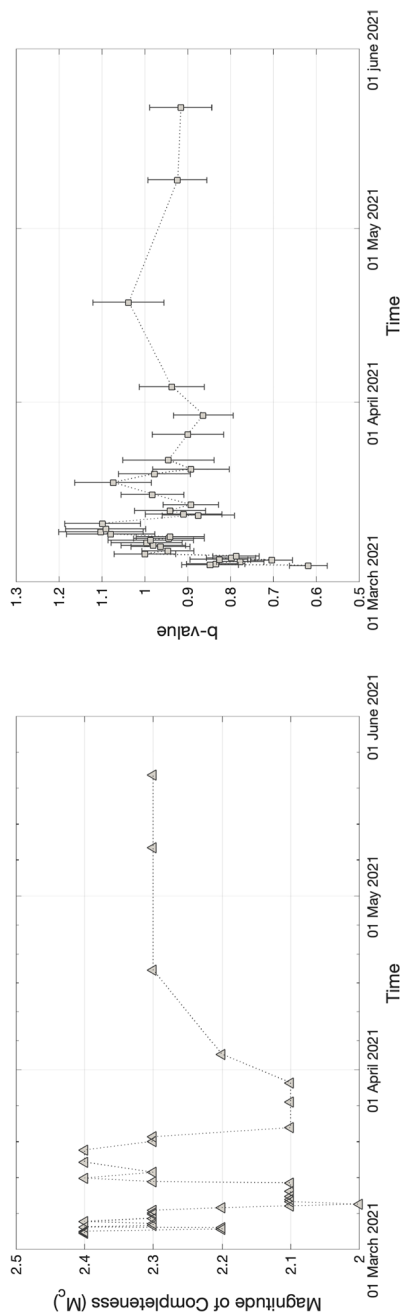


**Fig. 5** **a** The magnitude of completeness ( $M_c$ ) with time (triangles) as calculated with the maximum curvature method, in consecutive time windows of 200 events sliding every 50 events. **b** The estimated  $b$ -values of the G-R relation (squares) with time and their associated uncertainties, shown as error bars

### 3.2 Temporal properties of the aftershock sequence

#### 3.2.1 Aftershock production rate and modelling

Following the original observations by Omori in the late nineteenth century regarding the frequency of aftershocks following strong earthquakes in Japan (Omori 1894), the so-called Omori formula has been applied in numerous aftershock sequences ever since. This scaling relation is a manifestation of temporal correlations in aftershock sequences, which can be viewed as a complex relaxation process that follows a mainshock. Its modified version states that the aftershock production rate  $n(t) = dN(t)/dt$  (where  $N(t)$  is the number of aftershocks in time  $t$  after the mainshock) decays as a power-law with time  $t$  according to (Utsu et al. 1995):

$$n(t) = K(t + c)^{-p} \quad (2)$$

In the previous equation,  $K$  is a proportionality constant that depends on the total number of aftershocks,  $c$  is a positive constant that takes the dimensions of time and  $p$  is the power-law exponent that usually takes values in the range  $0.9 < p < 1.6$  (Utsu et al. 1995). The previous parameters and essentially the aftershock production rate depend on various properties particular to the seismogenic region, such as the tectonic setting, the stress changes along the regional faults, the structural heterogeneities, and the crustal rheology (Utsu et al. 1995; Shcherbakov et al. 2004; Valerio et al. 2017).

The parameters  $K$ ,  $c$ , and  $p$  in the modified Omori formula are usually calculated with the MLE method (Ogata 1983). The likelihood function in this case for  $N$  aftershocks occurring at time  $t_i$   $\{i=1,2,\dots,N\}$  between  $T_1$  and  $T_2$  with intensity  $\lambda(t)=n(t)$  is written as (Ogata 1983):

$$L = \left\{ \prod_{i=1}^N \lambda(t_i) \right\} \exp \left\{ - \int_{T_1}^{T_2} \lambda(t) dt \right\} \quad (3)$$

The parameters in Eq. 2 are estimated by maximizing the function  $\ln L$ . In addition, the cumulative number of aftershocks  $N(t)$  is estimated from  $n(t)$  (Eq. 2) as:



$$N(t) = \int_0^t n(s)ds = \begin{cases} K[c^{1-p} - (t+c)^{1-p}]/(p-1), \text{for } p \neq 1 \\ K \ln(t/c + 1), \text{for } p = 1 \end{cases} \quad (4)$$

The temporal evolution of the 2021 Northern Thessaly aftershock sequence, in terms of the cumulative number of aftershocks ( $M \geq M_c$ ) that followed the  $M_w$  6.3 mainshock, is shown in Fig. 6, along with the modified Omori formula (Eq. 4). For the entire sequence, the MLE for the modified Omori formula provides the parameters  $K = 670.6 \pm 227.0$ ,  $c = 1.51 \pm 0.37$  and  $p = 1.49 \pm 0.10$  (Table 2). For this set of parameters, the Akaike information criterion (Akaike 1974) provides the value of  $-5471$ , while

a two-sample Kolmogorov–Smirnov test does not reject the null hypothesis that the observed  $N(t)$  follows the modified Omori formula for the previous parameter values at the 1% significance level (test statistic 0.062 and asymptotic  $p$  0.058).

However, since breaks are observed in the cumulative number of aftershocks that signify event-rate changes in the production of aftershocks, particularly after the occurrence of strong  $M > 5$  events (Fig. 6), we also investigate the alternative hypothesis that strong events trigger their own aftershocks within the same aftershock sequence. In this case, the aftershock production rate  $n(t)$  can be expressed

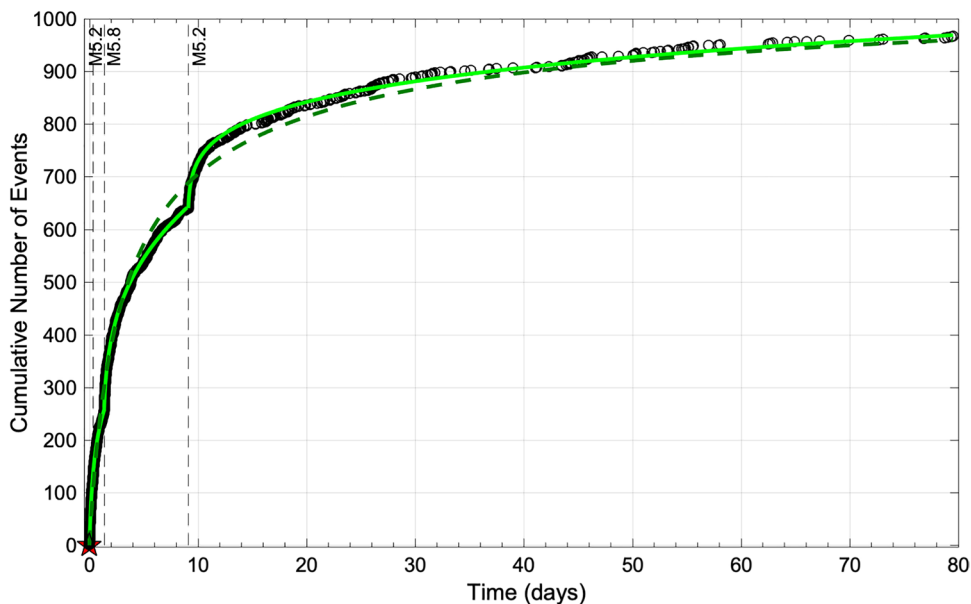


**Fig. 6** The cumulative number of events for  $M \geq M_c$  (symbols) with time that followed the  $M_w$  6.3 mainshock (star). The solid line represents the composite model of three modified Omori regimes, while the dashed line the model for a single modified

Omori regime. Vertical dashed lines mark the time of occurrence of the strongest earthquakes following the mainshock ( $M$  values after the AUTH bulletins)

**Table 2** The considered mainshock, the duration (in days), the number of events ( $N$ ), and the MLE of the modified Omori formula parameters for each case, along with their associated uncertainties. AIC is the estimated Akaike information crite-

rior for each model. The first row shows the results for a single modified Omori regime, while the last three rows for the composite model of three modified Omori regimes, presenting a unique AIC value

Model	Mainshock	Duration (days)	$N$	$K$	$c$ (days)	$p$	AIC
Single model	$M_w$ 6.3 03/03/21	80 days	967	$670.6 \pm 227.0$	$1.51 \pm 0.37$	$1.49 \pm 0.10$	$-5471$
Composite model	$M_w$ 6.3 03/03/21	1.35 days	254	$105.7 \pm 22.1$	$0.16 \pm 0.07$	$1.11 \pm 0.21$	$-5756$
	$M_w$ 6.0 04/03/21	7.63 days	385	$79.2 \pm 4.5$	$0.04 \pm 0.03$	$0.70 \pm 0.06$	
	$M_w$ 5.5 12/03/21	70.4 days	328	$36.1 \pm 3.5$	$0.03 \pm 0.02$	$0.81 \pm 0.04$	

as a combination of several modified Omori regimes (Ogata 1983; Utsu et al. 1995):

$$n(t) = K_1(t + c_1)^{-p_1} + H(t - t_2)K_2(t - t_2 + c_2)^{-p_2} + H(t - t_3)K_3(t - t_3 + c_3)^{-p_3} \quad (5)$$

where  $H(\cdot)$  represents a unit step function and  $t_2, t_3$  designate the occurrence times of secondary aftershock sequences. For times  $t < t_2$  and  $t < t_3$ , the parameters  $K_2$  and  $K_3$  in Eq. 5 equal zero, respectively. By setting  $t_2 = 1.35$  days and  $t_3 = 9.11$  days, which are the times from the mainshock when the second major event of  $M_w$  6.0 and the largest aftershock of  $M_w$  5.5 occurred, we model the three sequences individually and then together as a composite sequence, in which the aftershocks of each mainshock contribute to the event rate of the next sequence. The composite model, as estimated from the MLE for the three individual modified Omori regimes, is shown in Fig. 6. The duration of each sub-sequence, the number of events included (for  $M \geq M_c$ ), the estimated parameters of the corresponding modified Omori regime and their associated uncertainties are displayed in Table 2. After the occurrence of the  $M_w$  6.3 mainshock and up to the  $M_w$  6.0 second major event, a  $p$ -value of  $1.11 \pm 0.21$  is obtained. After the occurrence of the second major event and up to the  $M_w$  5.5 aftershock,  $p$ -value reduces to  $0.70 \pm 0.06$ , while thereafter we estimate the  $p$ -value of  $0.81 \pm 0.04$ . A visual inspection of Fig. 6 indicates that the composite model (Eq. 5) describes better the observed  $N(t)$  than the single modified Omori regime, which is further confirmed by the smaller AIC value of  $-5756$  (Table 2) that the composite model presents. In this case, the two-sample Kolmogorov–Smirnov test does not reject the null hypothesis that the observed  $N(t)$  follows the composite model for the parameter values listed in Table 2 at the 1% significance level, with a test statistic of 0.016 and asymptotic  $p$  of 0.999.

### 3.2.2 The waiting-times distribution

In addition, we study the temporal correlation properties of the aftershock sequence and construct the distribution of waiting times (or interevent times) between the successive aftershocks. In this analysis, earthquakes are considered as a point process in time, marked by the magnitude of the event, with waiting times  $\tau$  between the successive events defined

as  $\tau_i = t_{i+1} - t_i$ , where  $t_i$  is the time of occurrence of the  $i$ th event  $\{i = 1, 2, \dots, N-1\}$  and  $N$  the total number

of events. To investigate the probability distribution  $p(\tau)$ , the histogram of waiting times  $\tau$  is constructed, preferably in logarithmically spaced bins, as waiting times expand in a wide range of scales, varying between seconds, to hours and days. Then,  $p(\tau)$  is estimated by counting the number of  $\tau$  that fall in each bin, further normalized with the bin width, and divided by the total number of counts (e.g., Corral 2004; Michas and Vallianatos 2018).

Various models have been proposed to describe the distribution of waiting times between successive earthquakes. These models vary between complete randomness (e.g., homogeneous Poisson model), semi-randomness in which random background activity of mainshocks is interspersed by correlated aftershock sequences (e.g., ETAS model) and other models that indicate correlated earthquakes at all timescales (e.g., Michas and Vallianatos 2021 and references therein). Shcherbakov et al. (2005) suggested a non-homogeneous Poisson process to describe the observed scaling of aftershock sequences. On the other hand, the validity of the modified Omori formula (Eq. 2) implies that for a non-stationary Poisson process the waiting time distribution for correlated aftershock sequences scales as a power-law with exponent  $2-1/p$  (Utsu et al. 1995). In addition, for stationary seismicity rates the waiting time distributions of regional seismicity are well approximated by a generalized gamma function (Corral 2004), while for nonstationary earthquake time series a crossover behavior between two power-law regimes has been observed (Corral 2003; Michas et al. 2013; Michas and Vallianatos 2018). Michas and Vallianatos (2018) suggested a stochastic dynamic model with memory effects that produces the scaling behavior of nonstationary earthquake time series. The solution of this model is the so-called  $q$ -generalized gamma distribution that has the form:

$$f(\tau) = C \left( \frac{\tau}{\tau_0} \right)^{\gamma-1} \exp_q \left( -\frac{\tau}{\tau_0} \right) \quad (6)$$

where  $C$  is a normalization constant,  $\tau_0$  a scaling parameter and  $\gamma$  a scaling exponent, while the last term in the right-hand side of the equation is the  $q$ -exponential function:

$$\exp_q(x) = [1 + (1 - q)x]^{1/(1-q)} \tag{7}$$

For  $q > 1$ , the  $q$ -exponential function exhibits asymptotic power-law behavior, while in the limit  $q \rightarrow 1$  it recovers the ordinary exponential function and thus the  $q$ -generalized gamma distribution the ordinary gamma distribution. The  $q$ -exponential family of distributions are known from Non-Extensive Statistical Mechanics (NESM) (Tsallis 2009) and have found wide applications in the temporal scaling properties of seismic sequences (Vallianatos et al. 2016, 2018; Vallianatos and Michas 2020 and references therein), including aftershock sequences (Vallianatos et al. 2012).

Figure 7 shows the normalized probability density  $p(\tau)$  of waiting times  $\tau$  for the 2021 Northern Thessaly aftershock sequence. For the construction of  $p(\tau)$ , we considered only earthquakes with magnitude  $M \geq M_c$  and  $\tau \geq 60$  s. For waiting times less than 60 s a

rollover appears in  $p(\tau)$  that can be related to possible incompleteness of the catalogue at short time intervals due to overlapping of the recorded earthquakes in the seismograms (de Arcangelis et al. 2018). Short waiting times occur mainly in the early days of the aftershock sequence due to greater aftershock production rate and longer waiting times in the later part of the sequence where the production rate is lower (see Fig. 6).

The normalized probability density  $p(\tau)$  for the 2021 Northern Thessaly aftershock sequence shows a crossover behavior between two power-law regimes, in which long waiting times decay faster than short ones (Fig. 7). This scaling behavior can well be approximated with the  $q$ -generalized gamma distribution (Eq. 6), for the parameter values of  $C = 0.18 \pm 0.02$ ,  $\tau_0 = 26.8 \pm 21.2$ ,  $\gamma = 0.28 \pm 0.09$  and  $q = 1.96 \pm 0.19$  (Fig. 7). The latter suggests temporal correlations in the evolution of the aftershock sequence at all time scales, in contrast to a homogeneous Poisson process where earthquakes occur randomly in time. In addition, the modified Omori formula (Eq. 8) implies that for a non-stationary Poisson process the waiting time distribution for

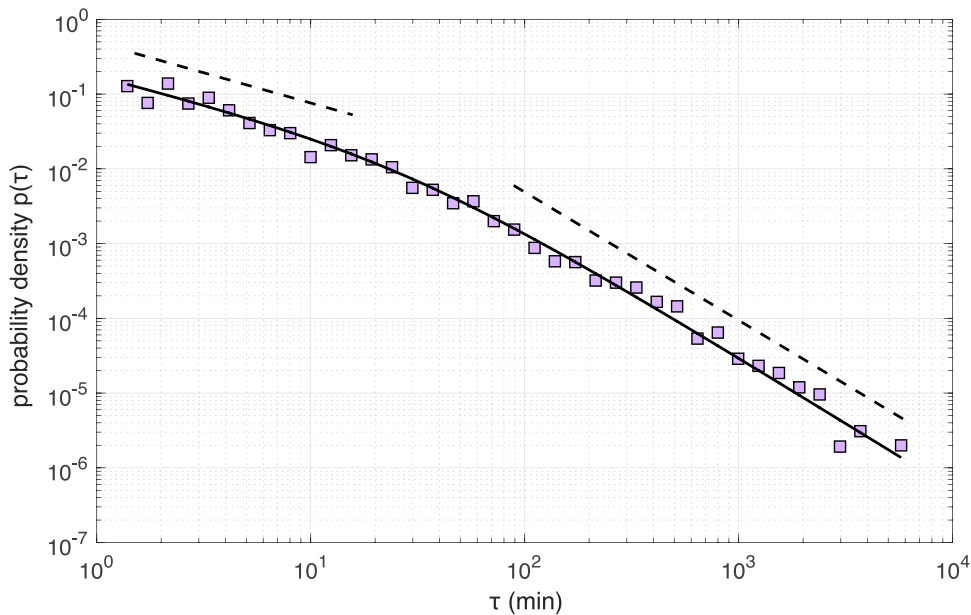


**Fig. 7** Normalized probability density  $p(\tau)$  of waiting times  $\tau$  for the 2021 Northern Thessaly aftershock sequence (filled symbols). The solid line represents the  $q$ -generalized gamma distribution (Eq. 6) for the parameter values  $C = 0.18$ ,  $\tau_0 = 26.8$ ,

$\gamma = 0.28$ , and  $q = 1.96$ . The dashed lines show the two power-law regimes for short and long waiting times, projected as straight lines in the log–log axis representation of the graph

correlated aftershock sequences scales as a power-law with exponent  $2-1/p$  (Utsu et al. 1995). For the entire sequence, we find  $p \approx 1.49$ , which implies the power-law exponent of  $\approx 1.3$  for the waiting time distribution. However, the observed  $p(\tau)$  presents a bimodal behavior and the crossover between two power-law regimes for short and long waiting times, which may be attributed to the various Omori regimes that are observed in the evolution of the aftershock sequence (Fig. 6).

#### 4 Spatial footprint of Coulomb stress changes

Various studies have shown a good correlation between positive Coulomb stress changes and the spatial evolution of most and significant aftershocks (e.g., King et al. 1994; Toda et al. 1998; King and Cocco 2001). The spatial distribution of the 2021 Northern Thessaly aftershock sequence (Fig. 2) shows an evolution of major aftershocks mainly towards the northwest. In this area the second major event of  $M_w$  6.0 and a major aftershock of  $M_w$  5.0 occurred on March 4, 2021, 18:38:18 (UTC) and 19:23:52 (UTC), respectively (Fig. 2). In this section, we study the aftershocks spatial distribution with respect to co-seismic static stress changes released during the  $M_w$  6.3 mainshock, as well as during the  $M_w$  6.0 s major event and the  $M_w$  5.5 major aftershock that took place 1 and 9 days later.

The Coulomb failure stress changes ( $\Delta CFS$ ) for undrained rock conditions are given by the difference between the static shear stress changes ( $\Delta\tau$ ) and the product of the effective normal stress changes ( $\Delta\sigma$ ) acting on the fault and the effective coefficient of friction ( $\mu_f$ ), as follows (e.g., Scholz 2019):

$$\Delta CFS = \Delta\tau - \mu_f \Delta\sigma \quad (8)$$

Positive changes of  $\Delta CFS$  advance failure, while negative changes of  $\Delta CFS$ , the so-called stress shadows, impede failure.

The effective coefficient of friction  $\mu_f$  in Eq. 8 intends to include the effects of pore-pressure changes (e.g., King et al. 1994). For an isotropic and homogeneous medium,  $\mu_f = \mu(1 - B)$ , where  $\mu$  is the coefficient of friction and  $B$  the Skempton's coefficient ( $0 < B < 1$ ) that describes the pore-pressure changes caused by an externally applied stress and frequently takes values within the range of 0.5 to 0.9 (Cocco and Rice 2002). For the determination of the co-seismic static stress changes, we used a mean value for the coefficient of friction equal to  $\mu_f = 0.4$  that is approximately the friction value for major faults (Harris and Simpson 1998). We considered this value to be sufficient for the calculations, as considerable differences from this value do not seem to substantially alter the distribution of  $\Delta CFS$  surrounding a fault (King et al. 1994).

To account for a realistic finite fault model for the major events, we considered the available focal mechanism solutions provided by various agencies and also by Karakostas et al. (2021) and Ganas et al. (2021). Our preferred models for the three earthquakes are listed in Table 3. For the  $M_w$  6.3 mainshock, we adopted the fault model of Karakostas et al. (2021), while for the  $M_w$  6.0 s major event and the  $M_w$  5.5 aftershock we used the fault models as derived from the median values of moment tensor inversions reported by various international agencies (Ganas et al. 2021). To determine the subsurface fault's length and width, we further used the empirical relations of Wells and Coppersmith (1994) for each modelled earthquake (e.g., Lin and Stein 2004; Toda et al. 2005). The calculations were performed

**Table 3** Focal parameters of the two main earthquakes and the major aftershock during the 2021 Northern Thessaly seismic sequence

Date	Time (GMT)	Depth (km)	$M_0$ (Nm)	$M_w$	Latitude	Longitude	Strike/Dip/Rake1 (°)	SRL <sup>†</sup> (km)	RW <sup>†</sup> (km)
3/3/2021	10:16:08	9.5	2.20E+18	6.3	39.7349	22.1908	314/36/−88*	18.74	11.78
4/3/2021	18:38:18	11	1.30E+18	6.0	39.78	22.12	298/36/−92**	11.97	8.49
12/3/2021	12:57:50	10	2.25E+17	5.5	39.8281	22.0150	108/40/−108**	5.67	4.92

\* Source: Karakostas et al. (2021); \*\* median values as reported in Ganas et al. (2021); † SRL subsurface rupture length, RW down-dip rupture width

at the depth of 9.5 km, which is the focal depth of the  $M_w$  6.3 mainshock (Table 3).  $\Delta$ CFS changes were calculated with the Coulomb3.3 software (Toda et al. 2011) in an elastic half-space, assuming a uniform slip on the rupture planar surfaces that imposes an “ideal” stress redistribution around the seismic faults. For the shear modulus and Poisson’s ratio, we further assumed the values of 3.3 MPa and 0.25, respectively. The calculated  $\Delta$ CFS changes for the preferred fault models were further examined in comparison to the spatial distribution of the relocated hypocenters of the sequence, as estimated by Karakostas et al. (2021) for the period March 03–April 04, 2021.

The calculated co-seismic  $\Delta$ CFS changes produced by the  $M_w$  6.3 mainshock at the centroid depth of 9.5 km are shown in Fig. 8. The spatial distribution of the static Coulomb stress changes reveals stress decrease towards NE and SW and stress loading up to 2 bars (0.2 MPa) towards NW and SE of the ruptured fault. Most aftershocks during the first day after the mainshock and up to the occurrence of the second major event on March 4, shown as green circles in Fig. 8, are mainly distributed along the ruptured fault, but also along the NW and SE positive lobes, particularly at the two edges of the ruptured fault as the cross-sections also reveal (Fig. 8). In the NW-positive lobe produced by the  $M_w$  6.3 mainshock, the second major event of  $M_w$  6.0 occurred one day later. Figure 9 shows the corresponding co-seismic  $\Delta$ CFS changes produced by the  $M_w$  6.0 event at the depth of 9.5 km. Stress loading up to 1 bar (0.1 MPa) appears, in this case, towards NW and SE of the ruptured fault. After the second major event and within 45 min, a strong aftershock of  $M$  5.1 occurred in the NW positive lobe. In the same area and within the NW positive lobe, another strong aftershock of  $M_w$  5.5 occurred on March 12, 2021, 8 days after the  $M_w$  6.0 event. The spatial distribution of the aftershocks after the  $M_w$  6.0 event and up to the  $M_w$  5.5 aftershock, shown as green circles in Fig. 9, as well as the vertical cross-sections in Fig. 9, indicates that the aftershock activity propagates mainly along the second ruptured fault and towards the positive stressed areas. In Fig. 10, we also show the calculated co-seismic  $\Delta$ CFS changes produced by the  $M_w$  5.5 strongest aftershock. In this case, a SSW-dipping normal fault is activated, antithetic to the previous ones that ruptured during the two major events. Stress loading up to 1 bar (0.1 MPa) appears after the  $M_w$  5.5

aftershock towards WNW and ESE of the ruptured fault (Fig. 10). Once more we observe that most aftershocks that occurred after the  $M_w$  5.5 event are distributed towards the positive stressed areas. The C-D vertical cross-section (Fig. 10), in particular, shows how aftershocks are aligned along the activated structure and the stress-loaded areas.

From the calculation of the co-seismic  $\Delta$ CFS changes, we thus observe that most aftershocks, including those of greater magnitude, occurred within positive static stress changes produced by the two major earthquakes of March 3 and 4, respectively, and by the strongest aftershock of March 12, 2021. The latter implies that the spatial distribution of aftershocks, including those of greater magnitude, is controlled by the co-seismic Coulomb stress changes produced during the  $M_w$  6.3 mainshock and the major events of the sequence.

## 5 Discussion

The occurrence of significant earthquakes provides the opportunity to study their statistical properties and test existing and novel models for the evolution of aftershock sequences that follow the mainshock. In this study, a detailed statistical analysis of the 2021 Northern Thessaly aftershock sequence was performed to study the frequency–magnitude distribution and its temporal properties. The temporal decay of the aftershock production rate and the distribution of earthquake magnitudes, in particular, form the basic components of short-term probabilistic forecasting models that are routinely used to constrain the magnitudes of the largest expected aftershocks and assess the associated hazard and risk (e.g., Reasenber and Jones 1989; Omi et al. 2013; Shcherbakov 2021).

The statistical analysis has indicated that the 2021 Northern Thessaly aftershock sequence exhibits scaling in the distribution of earthquake magnitudes and in its temporal evolution. The frequency–magnitude distribution is well constrained with the G-R relation (Eq. 1), presenting the  $b$ -value of  $0.90 \pm 0.03$ , which is typical for tectonic earthquakes (Schorlemmer et al. 2005) and almost identical to  $b=0.91$  for aftershock sequences in California (Reasenber and Jones 1989). The  $b$ -value of the aftershock sequence is almost comparable to the longer-term value of  $b=0.96$  for Northern Thessaly (Vamvakaris et al.

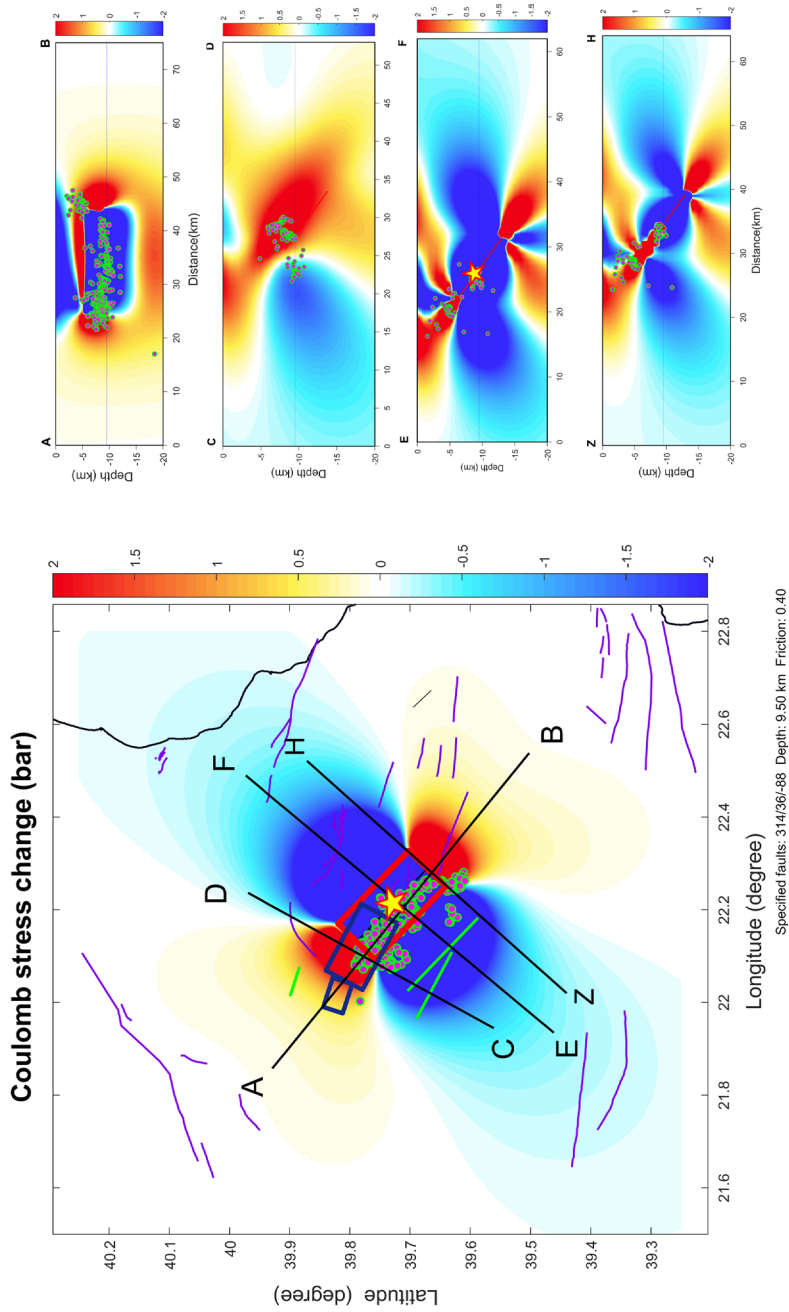


**Fig. 8** (Left) Coulomb stress changes produced by the  $M_w$  6.3 mainshock (yellow star) at centroid depth of 9.5 km. The red rectangle shows the fault model for the kinematics listed in Table 3 for the  $M_w$  6.3 event. (Right) Coulomb stress changes along the vertical cross-sections shown in the left panel. The solid green lines show the surface projections of the fault models, while the green circles show the relocated hypocenters of the aftershocks (after Karakostas et al. 2021) that occurred after the mainshock and up to the occurrence of the second major event on March 4, 2021

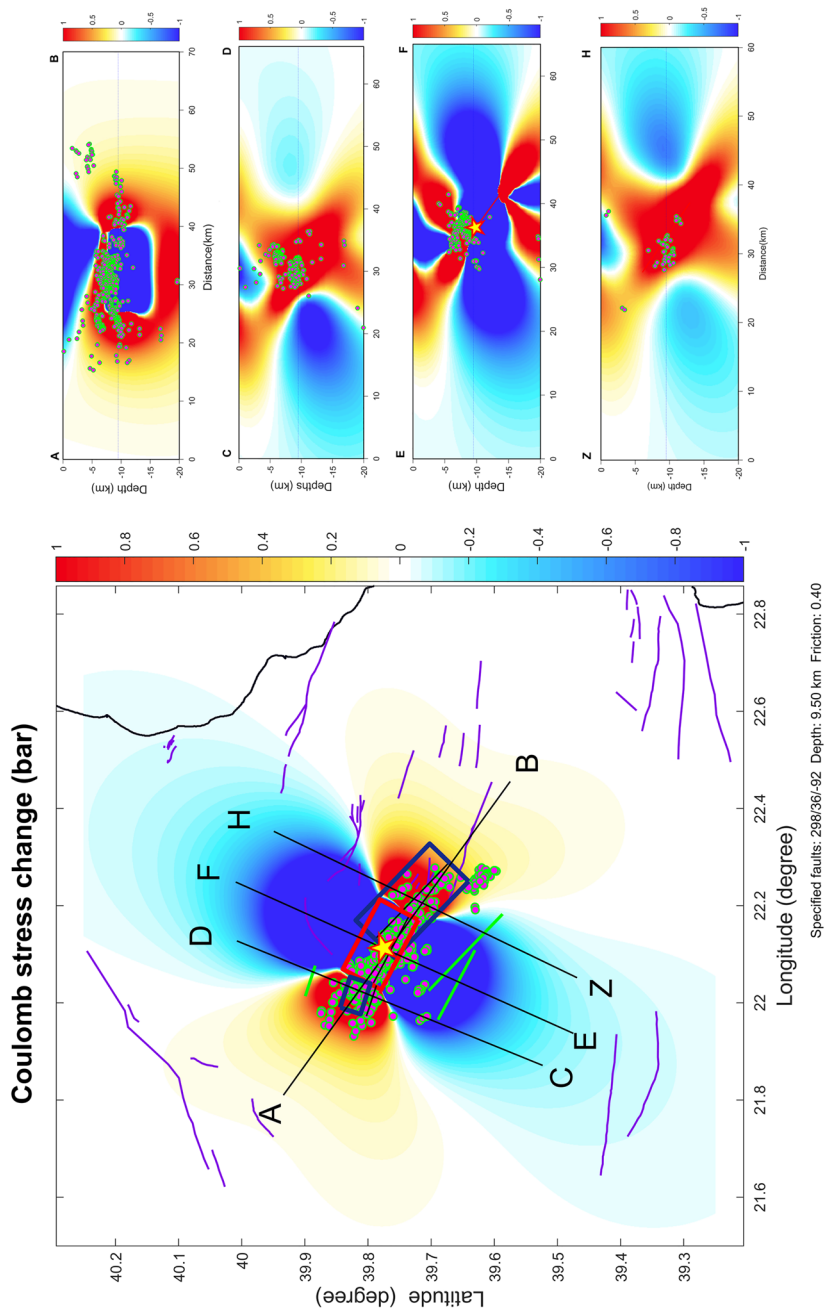


**Fig. 9** (Left) Coulomb stress changes produced by the  $M_w$  6.0 second major event (yellow star), at centroid depth of 9.5 km. The red rectangle shows the fault model for the kinematics listed in Table 3 for the  $M_w$  6.0 event. (Right) Coulomb stress changes along the vertical cross-sections shown in the left panel. The solid green lines show the surface projections of the fault models, while the green circles show the relocated hypocenters of the aftershocks (after Karakostas et al. 2021) that occurred after the  $M_w$  6.0 event and up to the occurrence of the  $M_w$  5.5 aftershock on March 12, 2021

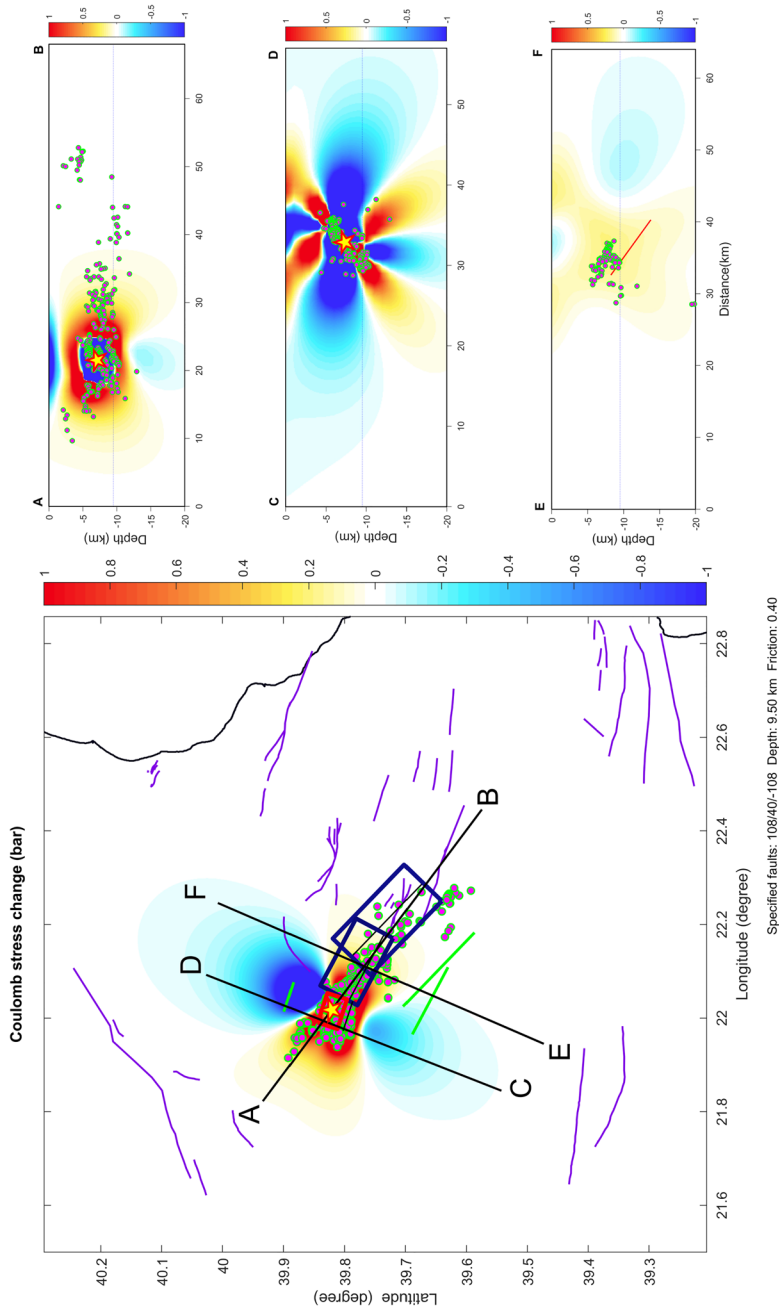


**Fig. 10** (Left) Coulomb stress changes produced by the  $M_w$  5.5 major aftershock (yellow star), at centroid depth of 9.5 km. The red rectangle shows the fault model for the kinematics listed in Table 3 for the  $M_w$  5.5 event. (Right) Coulomb stress changes along the vertical cross-sections shown in the left panel. The solid green lines show the surface projections of the fault models, while the green circles the relocated hypocenters of aftershocks (after Karakostas et al. 2021) that occurred after the  $M_w$  5.5 event and up to April 4, 2021



2016), but about ~20% less than the regional  $b$ -value during 2011–2020, a 10-years period prior to the 2021 mainshock. As the  $b$ -value is a manifestation of the relative number of small to large earthquakes, the latter indicates the relative absence of larger magnitude earthquakes in the broader epicentral area during the last decade prior to the 2021 mainshock. The much smaller value of  $b=0.62\pm 0.04$  that appears during the first hours after the  $M_w$  6.3 mainshock (Fig. 5) indicates the systematic lack of small-magnitude earthquakes, which can be attributed to missed events during the early post seismic period. In later times and after the installation of the local network on March 5th, more aftershocks are recorded, establishing the overall  $b$ -value of  $0.90\pm 0.03$  for the aftershock sequence.

The temporal decay rate of aftershocks was modelled with the modified Omori formula (Eq. 2), indicating that a composite model of three superimposed modified Omori regimes describes better the decay rate of aftershocks. This pattern of large aftershocks triggering their own sequences seems to be quite frequent in aftershock sequences in Greece (Drakatos and Latoussakis 1996). The estimated  $K$  parameters (Eq. 2) that describe the productivity of the sequence indicate that aftershock productivity was higher after the  $M_w$  6.3 mainshock and gradually decreased after the  $M_w$  6.0 second major event and the  $M_w$  5.5 aftershock (Table 2). The parameter  $c$  represents a characteristic time that usually reflects the incompleteness of the recorded events immediately after the mainshock (Kisslinger and Jones 1991; Kagan 2004). If such the case, then the reduced  $c$  parameters that are estimated after the  $M_w$  6.0 event and the  $M_w$  5.5 aftershock (Table 2) could manifest the increased ability of the network to detect small-magnitude earthquakes, following the installation of the local network on March 5th. The  $p$ -value also shows a decrease from  $1.11\pm 0.21$ , after the  $M_w$  6.3 mainshock, to  $0.70\pm 0.06$  and  $0.81\pm 0.04$ , after the occurrence of the second major event and the  $M_w$  5.5 aftershock, respectively, indicating a systematic decrease of the decay rate of aftershocks with time. A similar decrease in the estimated  $p$ -values has also been observed after the second major event during the 2010 Efpalio earthquake sequence that occurred in the western Corinth Rift, Greece (Michas 2016). During the 2016 Kumamoto, Japan, and 2019 Ridgecrest, USA, aftershock sequences, however, that both

presented pronounced foreshock sequences triggered by strong foreshocks of magnitudes  $M$  6.5 and  $M$  6.4, followed by mainshocks of magnitudes  $M$  7.3 and  $M$  7.1, respectively, both of strike-slip mechanisms, the  $p$ -values were smaller during the foreshock period that preceded the mainshocks than the aftershock sequences that followed them (Nanjo et al. 2019; Shcherbakov 2021). Such changes might be related to changes in the stress field that preceded and followed the mainshocks (Nanjo et al. 2019).

Furthermore, the analysis regarding the co-seismic Coulomb stress changes that followed the major events of the sequence showed a strong spatial correlation between stress-loaded areas and the spatial distribution of aftershocks. In the following, we investigate an additional physical mechanism for the spatiotemporal evolution of the aftershock sequence, based on afterslip propagation along the ruptured fault. Initially, we apply principal component analysis to the spatial distribution of the epicenters to define the geometry and the growth patterns of the aftershocks zone. Then, we study the expansion of the aftershock zone in terms of rate strengthening rheology that governs the evolution of the afterslip process.

## 5.1 Spatial distribution of aftershocks

### 5.1.1 Aftershocks focal zone growth

To quantify the focal zone size of the aftershock sequence and its temporal evolution, we perform the statistical method of principal component analysis (PCA). PCA is an efficient technique of multivariate analysis that is widely used to find patterns in large datasets and to reduce their dimensionality (Jolliffe 2002; Jackson 2003). Herein, we use PCA to quantify the geometry of the aftershocks' spatial distribution. We restrict the analysis to 2D and the aftershock epicenters, as in the AUTH earthquake catalogue that is used the depths are less well constrained. The coordinates of the aftershock epicenters are diagonalized to estimate the eigenvalues and eigenvectors of the covariance matrix that define the axes of an ellipse that includes at least 95% of all aftershocks. We fix the origin time to the  $M_w$  6.3 mainshock and perform the analysis in increasing time windows to calculate the temporal changes in the area and semiaxis lengths of the best fitting ellipse. The (0,0) origin is set in

each time window at the mean location of the aftershocks cloud.

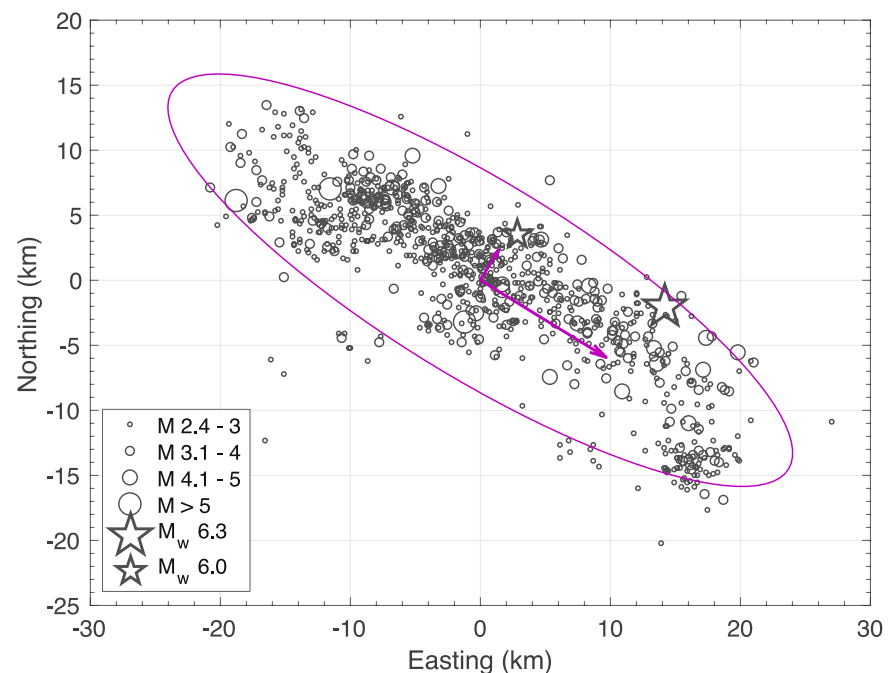
After the surpass of 80 days following the  $M_w$  6.3 mainshock, the activated zone, as approximated by the best fit ellipse, occupies an area of 653.5 km<sup>2</sup> (Fig. 11). The lengths of the 1<sup>st</sup> and 2<sup>nd</sup> principal semiaxes are ~28 km and ~7.5 km, respectively. The direction of the 1<sup>st</sup> principal semiaxis that points towards the maximum spatial variance is N121.5° E (Fig. 11), in close agreement with the focal mechanisms of the two major events (Fig. 2), the NW–SE regional tectonic setting (Fig. 1) and the positive coseismic Coulomb stress changes (Figs. 8 and 9). The results of the analysis regarding the temporal changes in the area and the semiaxis lengths of the ellipses that best fit the aftershocks cloud are shown in Fig. 12, in successive time windows that increase by one day. The activated area and the length of the 1<sup>st</sup> principal semiaxis are growing constantly during the first 10 days after the mainshock and remain almost constant thereafter. A great fraction, reaching ~80% of the total area, was seismically activated immediately after the mainshock and during the first day, while during the second day, the activated zone reached ~90% of the total area (Fig. 12). The length of the 2<sup>nd</sup> principal semiaxis reached its maximum during the first day and remained constant throughout

the aftershock sequence. The previous observations indicate that postseismic deformation following the  $M_w$  6.3 mainshock can well be described by only the 1<sup>st</sup> principal component in PCA, in agreement with the results of previous studies (Savage and Svarc 1997; Perfettini et al. 2010; Perfettini and Avouac 2014; Gualandi et al. 2016).

### 5.1.2 Scaling of the aftershocks focal zone with time

In the previous section, we discussed the expansion of the aftershocks focal zone with time, particularly during the first ten days following the mainshock. Such migration patterns of aftershocks with time are frequently, albeit not universally, observed (Tajima and Kanamori 1985; Henry and Das 2001; Helmstetter et al. 2003). It has widely been reported that the observed migration pattern of aftershocks scales as the logarithm of time (Peng and Zhao 2009; Obana et al. 2014; Tang et al. 2014; Frank et al. 2017; Perfettini et al. 2018; Vallianatos and Pavlou 2021). This semilogarithmic migration pattern implies that aftershocks are driven by afterslip, as suggested by numerical simulations (Ariyoshi et al. 2007; Kato 2007), and observed in real cases (Peng and Zhao 2009; Perfettini et al. 2018). Perfettini et al. (2018) have recently introduced a

**Fig. 11** Spatial distribution of the aftershock sequence in km (grey circles), centered to the mean location of the earthquakes' epicenters. The principal components derived with PCA define the principal axes of an ellipse (solid line) that includes at least 95% of all aftershocks. The arrows point to the direction of the principal semiaxes of the ellipse



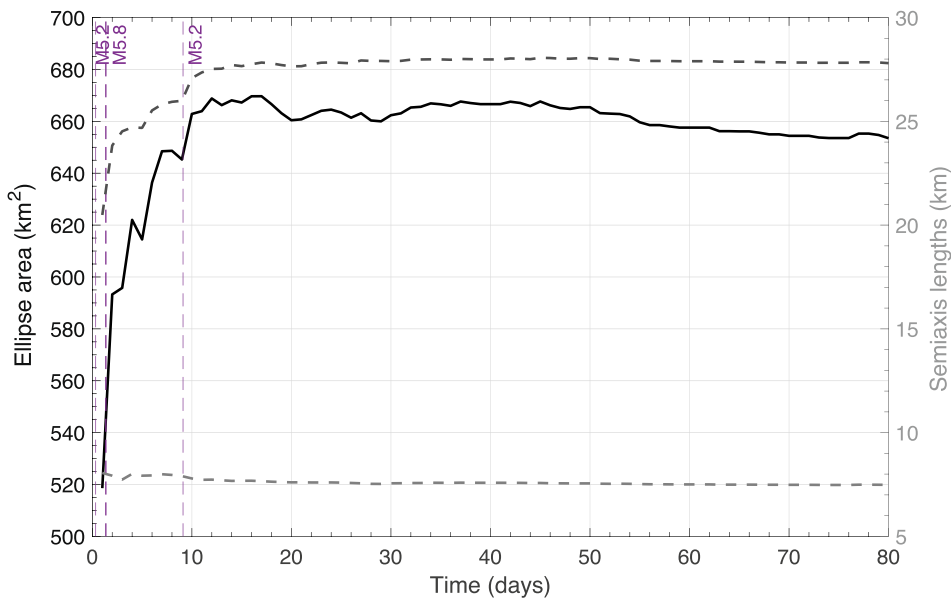


**Fig. 12** Temporal evolution (in days) of the aftershocks area (solid line; left y-axis) following the  $M_w$  6.3 mainshock, defined by an ellipse that includes at least 95% of all aftershocks. The temporal evolution in semiaxis lengths of the

ellipse is shown with the dashed lines (right y-axis). Vertical dashed lines mark the time of occurrence of the strongest earthquakes following the mainshock

numerical model that incorporates aftershocks nucleation as the outcome of afterslip propagation along the fault, to predict the aftershocks zone expansion. The model initially considers that asperities on a fault are stressed during the inter-seismic phase by regional creep occurring at a steady deformation rate. Some asperities slip co-seismically as the mainshock occurs, transferring large positive Coulomb stresses to the surrounding creeping regions. These stress-loaded regions accommodate large amounts of afterslip during the post-seismic phase. When a critical level of afterslip is reached, aftershocks are triggered along the fault. The model further assumes that co-seismic static stress changes trigger aftershocks only during the early post-seismic phase so that the larger fraction of aftershocks is driven by afterslip.

In the model introduced by Perfettini et al. (2018), aftershocks are thus produced by afterslip loading the asperities (see also Perfettini and Avouac 2004). Following Perfettini et al. (2018), the seismicity rate  $R(t)$  may then be proportional to the rate of afterslip  $V(t)$  in the same area, given by:

$$V(t) = \frac{V_+ \exp\left(\frac{t}{t_r}\right)}{1 + \left(\frac{V_+}{V_L}\right) \left[ \exp\left(\frac{t}{t_r}\right) - 1 \right]} \tag{9}$$

where  $V_+$  is the sliding velocity just after the end of co-seismic rupture,  $V_L$  the long-term loading velocity after the mainshock, and  $t_r$  the duration of the post-seismic phase. Following the previous assumption, the seismicity rate  $R(t)$  is then given by:

$$R(t) = \frac{R_+ \exp\left(\frac{t}{t_r}\right)}{1 + \left(\frac{R_+}{R_L}\right) \left[ \exp\left(\frac{t}{t_r}\right) - 1 \right]} \tag{10}$$

with  $R_+$  and  $R_L$  being the seismicity just after the end of co-seismic rupture and the long-term seismicity rate after the mainshock, respectively. The parameters  $t_r$  and  $R_+$  are given by  $t_r = A/\dot{\tau}$  and  $R_+ = R_L \exp(\Delta CFS/A)$ , where  $\dot{\tau}$  is the stressing rate,  $\Delta CFS$  the co-seismic Coulomb stress change induced by the mainshock and  $A' = (a - b)\sigma$ , with  $a$  and  $b$  the rate and state frictional parameters and  $\sigma$  the

effective normal stress. The latter equation (Eq. 10), for  $t/t_r \ll 1$ , yields a  $1/t$  decay for  $R(t)$  (Perfettini and Avouac 2004), consistent with the modified Omori formula (Eq. 2) with  $p=1$ .

For modelling aftershock migration using the previous assumptions, a fault with only depth varying normal stress, stressing rate, and rheological parameter  $A'$  is considered. Aftershocks migrate along the strike direction  $x$ , assuming that the initial Coulomb stress field varies with  $x$ , forming the initial distribution of afterslip velocities. Focusing on the early stage of the post-seismic phase that typically lasts several weeks or months after the mainshock ( $t/t_r \ll 1$ ), the propagation velocity  $V_p$  of the aftershocks zone is given by (Perfettini et al. 2018):

$$V_p = \frac{A'}{t} \times \left( -\frac{\partial \Delta CFS}{\partial x} \right)^{-1} \quad (11)$$

The latter equation predicts that  $V_p$  decays as  $1/t$ . The expansion of the aftershocks zone  $L_a$  between time  $t_i$  and  $t$  ( $t > t_i$ ) is now given by:

$$\Delta L_a(t) = L_a(t) - L_a(t_i) = A' \times \left( -\frac{\partial \Delta CFS}{\partial x} \right)^{-1} \ln \left( \frac{t}{t_i} \right) \quad (12)$$

which predicts an expansion of the aftershocks zone as the logarithm of time. For a smooth co-seismic Coulomb stress field, the latter equation implies the slow migration of the aftershocks zone.

Since the estimated co-seismic Coulomb stress field  $\Delta CFS$  (Eq. 8) can be significantly different from the “real” one, Perfettini et al. (2018) suggested a mean Coulomb stress gradient to be used. In this case, Eq. 12 becomes:

$$\langle \Delta L_a(t) \rangle = A' \times \left( -\frac{\partial \Delta CFS}{\partial x} \right)^{-1} \ln \left( \frac{t}{t_i} \right) = \zeta A' \frac{l_c}{\Delta \sigma} \ln \left( \frac{t}{t_i} \right) \quad (13)$$

where  $l_c$  is the radius of the co-seismic rupture,  $\Delta \sigma$  the mean value of the mean co-seismic stress drop, and  $\zeta$  a constant. For an idealized Coulomb stress field (Dieterich 1994),  $\zeta$  takes the value of 2.77 (Perfettini et al. 2018).

In Fig. 13, we show the mean expansion of the aftershocks zone  $L_a$  with time for the 2021 Northern Thessaly aftershock sequence ( $M \geq M_c$ ), along the strike direction defined by the 1<sup>st</sup> principal component derived with PCA (see the previous section). As in Fig. 12, the expansion of the aftershocks zone becomes apparent, particularly during the first ten days following the mainshock. An acceleration in

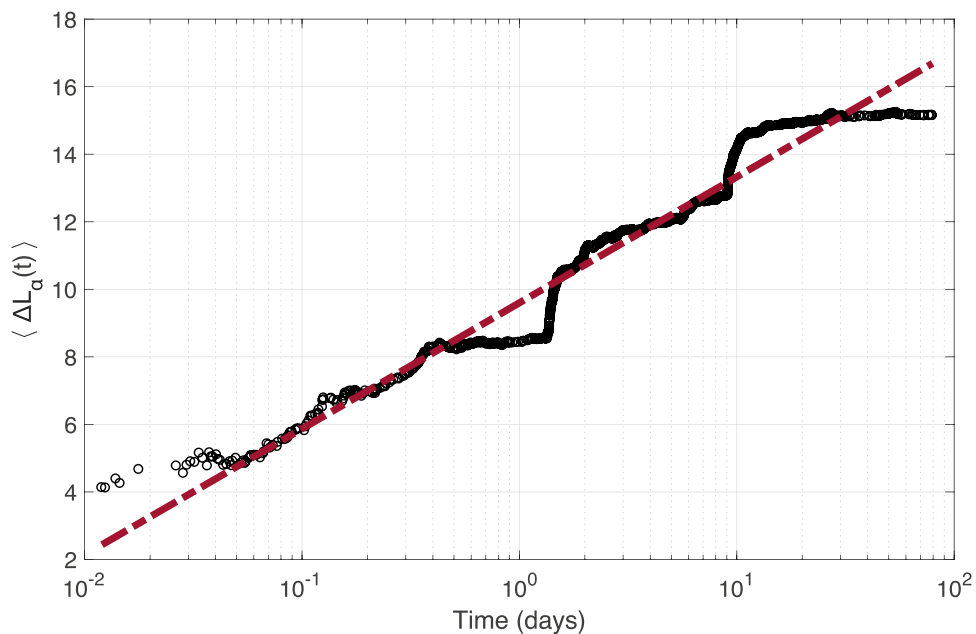


**Fig. 13** The mean distance (in km) of aftershocks from the  $M_w$  6.3 mainshock with time (open circles), along the 1<sup>st</sup> principal component derived with PCA. The dashed line represents the logarithmic growth of the aftershocks zone

expansion speed, signified by the step-like behavior in Fig. 13, also becomes evident after the occurrence of the second major event of  $M_w$  6.0 and the largest aftershock of  $M_w$  5.5, 1.35, and 9.11 days after the mainshock, respectively. The afterslip front, shown as a function of the logarithm of time according to Eq. 13, matches well the mean expansion of the aftershocks zone ( $R^2=0.96$ ), particularly during the first 10 days after the mainshock (Fig. 13).

In addition, if  $s_a$  is the slope of the afterslip front shown in Fig. 13, then from Eq. 13, we get  $s_a = \frac{d(L_a(t))}{d \ln t} = \zeta A' \frac{l_c}{\Delta \sigma}$ . From the latter equation, the rheological parameter  $A'$  can be determined, once rough estimates of the mean co-seismic stress drop  $\Delta \sigma$  and the radius of the co-seismic rupture  $l_c$  are known. For a simple model of circular rupture, the co-seismic source radius  $l_c$  can approximately be determined as  $l_c = \left(\frac{7 M_0}{2 \Delta \sigma}\right)^{1/3}$  (Eq. 4.16 of Scholz 2019). Taking the mainshock's seismic moment  $M_0=2.20 \cdot 10^{18}$  Nm (Table 3) and the average stress drop of  $\Delta \sigma=5.5 \pm 1.5$  MPa for normal fault earthquakes in Greece (Margaris and Hatzidimitriou 2002), we estimate the value of  $l_c \approx 11.2$  km for the co-seismic rupture. Eventually, for  $\zeta=2.77$ , the rheological parameter  $A'$  takes the value of  $A' \approx 0.29$  MPa, while for  $\zeta=1$ ,  $A' \approx 0.8$  MPa, which are within the range 0.1 – 1 MPa of  $A'$  values that are usually found (Perfettini et al. 2010). Perfettini and Avouac (2007) estimated  $A' \approx 0.5$  MPa for the 1992  $M_w$  7.3 Landers earthquake, while a similar  $A'$  value was proposed by Perfettini et al. (2018) for the 2011  $M_w$  9.0 Tohoku earthquake. On the other hand, Vallianatos and Pavlou (2021) estimated  $A' \approx 0.041$  MPa for the 2020  $M_w$  7.0 Samos earthquake, similar to  $A'=4 \times 10^{-2}$  MPa found by Frank et al. (2017) for the Central Chile subduction zone.

## 6 Conclusions

In this work, we studied the scaling properties and the triggering mechanisms of the 2021 Northern Thessaly aftershock sequence that followed the recent  $M_w$  6.3 strong shallow earthquake. During the first days after the mainshock, a second  $M_w$  6.0 strong event and numerous aftershocks were generated, with some exceeding  $M_w$  5.0. Aftershocks propagated along a NW–SE direction, consistent with the regional

tectonic setting and the focal mechanisms of the major events. The aftershock sequence exhibits scaling properties consistent with well-known empirical relationships for aftershocks. In particular, the frequency of aftershock magnitudes follows the Gutenberg-Richter scaling law for a  $b$ -value of  $0.90 \pm 0.03$ . The aftershocks production rate decays as a power-law with time according to a composite model of three Omori regimes, which signify the generation of secondary aftershock sequences due to the occurrence of strong events within the same sequence. The waiting times between the successive aftershocks also presents scaling and a decay pattern according to a crossover behavior between two power-law regimes for short and long waiting times, respectively. This bimodal scaling behavior can well be approximated with the  $q$ -generalized gamma distribution, signifying clustering effects and correlations between aftershocks at all time scales.

In addition, we studied postseismic relaxation as expressed by the spatial distribution of aftershocks. The analysis of the aftershocks' epicenters with PCA shows that postseismic activity can be described with an ellipse and by only the 1<sup>st</sup> principal component that strikes at N121.5° E and presents the semi-axis length of ~28 km. The aftershocks focal zone grows constantly during the first ten days after the mainshock and then remains almost constant, occupying a total area of ~653.5 km<sup>2</sup>. The spatial distribution of aftershocks, including those of greater magnitude, spreads along stress-enhanced areas, indicating that co-seismic static stress changes produced by the  $M_w$  6.3 mainshock and the  $M_w$  6.0 second major event are the driving mechanism of the aftershock sequence. However, the logarithmic migration of aftershocks with time along the principal direction of their spatial distribution, demonstrates that aftershocks may well be driven by afterslip following the main rupture. In terms of rate strengthening rheology that governs the evolution of the afterslip process, the latter provides a rough estimate of the fault's rheological parameter  $A' \approx 0.29$  MPa.

Overall, the results presented herein shed light on the self-similar nature of the aftershock generation process during the 2021 Northern Thessaly aftershock sequence, governed by power-laws in the distributions of seismic energy release and the temporal occurrence of aftershocks. In the spatial domain, aftershocks migrate mainly along fault strikes during

the early phase of post-seismic relaxation, as a combined effect of co-seismic stress changes and afterslip following the mainshock. Such properties and the derived parameters can be used to constrain models of aftershock occurrence, to assess seismic hazard, and to mitigate the associated risk.

**Acknowledgements** We would like to thank two anonymous reviewers and the Associate Editor for their constructive comments and suggestions that helped to improve the quality of this work. We would also like to thank V. Karakostas for kindly providing the relocated catalogue of the aftershock sequence used in the analysis of the Coulomb stress changes. The Generic Mapping Tools (GMT 5) software was used to plot some of the maps (Wessel et al. 2013). We acknowledge the support of this work by the project “HELPOS – Hellenic System for Lithosphere Monitoring” (MIS 5002697) which is implemented under the Action “Reinforcement of the Research and Innovation Infrastructure”, funded by the Operational Programme “Competitiveness, Entrepreneurship and Innovation” (NSRF 2014–2020) and co-financed by Greece and the European Union (European Regional Development Fund).

**Funding** This research is partially supported by the project “HELPOS – Hellenic System for Lithosphere Monitoring” (MIS 5002697) which is implemented under the Action “Reinforcement of the Research and Innovation Infrastructure”, funded by the Operational Programme “Competitiveness, Entrepreneurship and Innovation” (NSRF 2014–2020) and co-financed by Greece and the European Union (European Regional Development Fund).

**Availability of data and material** The earthquake catalogue dataset used in this study is available from the Geophysics Department, Aristotle University of Thessaloniki (<https://doi.org/10.7914/SN/HT>), at <http://geophysics.geo.auth.gr/ss/> (last accessed on June 8, 2021).

**Code availability** The code used to calculate the Coulomb Failure Stress changes is freely available from the online source cited in the text. All the other codes used in the analysis were developed in the MATLAB® environment and are available from the authors upon reasonable requests.

## Declarations

**Conflict of interest** The authors declare no competing interests.

## References

- Akaike H (1974) A new look at the statistical model identification. *IEEE Trans Autom Control* 19(6):716–723
- Ariyoshi K, Matsuzawa T, Hasegawa A (2007) The key frictional parameters controlling spatial variations in the

- speed of postseismic-slip propagation on a subduction plate boundary. *Earth Planet Sci Lett* 256:136–146
- Ben-Zion Y, Lyakhovskiy V (2006) Analysis of aftershocks in a lithospheric model with seismogenic zone governed by damage rheology. *Geophys J Int* 165(1):197–210
- Bornovas J, Rondogianni-Tsiambaou T (1983) Geological Map of Greece 1:500.000 (second edition). Institute of Geology and Mineral Exploration (IGME), Athens
- Caputo R (1990) Geological and structural study of the recent and active brittle deformation of the Neogene-Quaternary basins of Thessaly (Central Greece). *Sci Ann Aristotle Univ Thessaloniki* 12:252
- Caputo R, Pavlides S (1993) Late Cainozoic geodynamic evolution of Thessaly and surroundings (central-northern Greece). *Tectonophysics* 223:339–362
- Caputo R, Helly B, Pavlides S, Papadopoulos G (2004) Palaeoseismological investigation of the Tyrnavos fault (Thessaly, central Greece). *Tectonophysics* 394(1–2):1–20
- Caputo R, Pavlides S (2013) The Greek Database of Seismogenic Sources (GreDaSS), Version 2.0.0: a compilation of potential seismogenic sources ( $M > 5.5$ ) in the Aegean region. <https://doi.org/10.15160/unife/gredass/0200>. <http://gredass.unife.it/>. Accessed 8 June 2021
- Cocco M, Rice JR (2002) Pore pressure and poroelasticity effects in Coulomb stress analysis of earthquake interactions. *J Geophys Res Solid Earth* 107(B2):ESE-2
- Corral A (2004) Long-term clustering, scaling, and universality in the temporal occurrence of earthquakes. *Phys Rev Lett* 92:108501
- Corral A (2003) Local distributions and rate fluctuations in a unified scaling law for earthquakes. *Phys Rev E* 68
- D’Agostino N, Métois M, Koci R, Duni L et al (2020) Active crustal deformation and rotations in the southwestern Balkans from continuous GPS measurements. *Earth Planet Sci Lett* 539:116246. <https://doi.org/10.1016/j.epsl.2020.116246>
- Das S, Scholz CH (1981) Theory of time-dependent rupture in the Earth. *J Geophys Res Solid Earth* 86(B7):6039–6051
- de Arcangelis L, Godano C, Lippiello E (2018) The overlap of aftershock coda waves and short-term postseismic forecasting. *J Geophys Res Solid Earth* 123:5661–5674
- Dieterich JH (1972) Time-dependent friction as a possible mechanism for aftershocks. *J Geophys Res* 77:3771–3781
- Dieterich JH (1994) A constitutive law for earthquake production and its application to earthquake clustering. *J Geophys Res* 99:2601–2618
- Drakatos G, Latoussakis J (1996) Some features of aftershock patterns in Greece. *Geophys J Int* 126(1):123–134
- Frank WB, Poli P, Perfettini H (2017) Mapping the rheology of the Central Chile subduction zone with aftershocks. *Geophys Res Lett* 44:5374–5382. <https://doi.org/10.1002/2016GL072288>
- Frohlich C, Davis SD (1993) Teleseismic b values; or, much ado about 1.0. *J Geophys Res Solid Earth* 98(B1):631–644
- Ganas A, Valkaniotis S, Briole P, Serpetsidaki A, Kapetanidis V et al (2021) Domino-style earthquakes along blind normal faults in Northern Thessaly (Greece): kinematic evidence from field observations, seismology, SAR interferometry and GNSS. *Bull Geol Soc Greece* 58:37–86. <https://doi.org/10.12681/bgsg.27102>

- Gualandi A, Avouac J-P, Galetzka J, Genrich JF, Blewitt G, BijayaAdhikari L et al (2016) Pre- and post-seismic deformation related to the 2015, Mw 7.8 Gorkha earthquake. *Nepal Tectonophys* 714:90–106. <https://doi.org/10.1016/j.tecto.2016.06.014>
- Gutenberg B, Richter CF (1944) Frequency of earthquakes in California. *Bull Seismol Soc Am* 34(4):185–188
- Harris RA, Simpson RW (1998) Suppression of large earthquakes by stress shadows: a comparison of Coulomb and rate-and-state failure. *J Geophys Res Solid Earth* 103(B10):24439–24451
- Hatzfeld D, Ziazia M, Kementzetzidou D, Hatzidimitriou P, Panagiotopoulos D, Makropoulos K, Papadimitriou P, Deschamps A (1999) Microseismicity and focal mechanisms at the western termination of the North Anatolian Fault and their implications for continental tectonics. *Geophys J Int* 137(3):891–908
- Helmstetter A, Ouillon G, Sornette D (2003) Are aftershocks of large California earthquakes diffusing? *J Geophys Res Solid Earth* 108:2483. <https://doi.org/10.1029/2003JB002503>
- Henry C, Das S (2001) Aftershock zones of large shallow earthquakes: fault dimensions, aftershock area expansion and scaling relations. *Geophys J Int* 147(2):272–293
- Hsu YJ, Simons M, Avouac JP, Galetzka J, Sieh K, Chlieh M, Natawidjaja D, Prawirodirdjo L, Bock Y (2006) Frictional afterslip following the 2005 Nias-Simeulue earthquake, Sumatra. *Science* 312(5782):1921–1926
- Jackson JE (2003) A user's guide to principal components. Wiley
- Jolliffe IT (2002) Principal component analysis, 2nd edn. Springer, New York. <https://doi.org/10.1007/b98835>
- Kagan YY (2004) Short-term properties of earthquake catalogs and models of earthquake source. *Bull Seismol Soc Am* 94(4):1207–1228
- Karakostas V, Papazachos C, Papadimitriou E, Fomelis M, Kiratzi A et al (2021) The March 2021 Tyrnavos, central Greece, doublet (Mw6.3 and Mw6.0): aftershock relocation, faulting details, coseismic slip and deformation. *Bull Geol Soc Greece* 58:131–178. <https://doi.org/10.12681/bgsg.27237>
- Kato N (2007) Expansion of aftershock areas caused by propagating post-seismic sliding. *Geophys J Int* 168:797–808
- King GC, Stein RS, Lin J (1994) Static stress changes and the triggering of earthquakes. *Bull Seismol Soc Am* 84(3):935–953
- King GCP, Cocco M (2001) Fault interaction by elastic stress changes: new clues from earthquake sequences. In: *Advances in Geophysics* 44, Elsevier
- Kisslinger C (1996) Aftershocks and fault-zone properties. *Advances in Geophysics* 38. Academic Press, San Diego, pp 1–36
- Kisslinger C, Jones LM (1991) Properties of aftershock sequences in Southern California. *J Geophys Res* 96(B7):11947–11958
- Lin J, Stein RS (2004) Stress triggering in thrust and subduction earthquakes and stress interaction between the southern San Andreas and nearby thrust and strike-slip faults. *J Geophys Res Solid Earth* 109(B2)
- Margaris BN, Hatzidimitriou PM (2002) Source spectral scaling and stress release estimates using strong-motion records in Greece. *Bull Seismol Soc Am* 92(3):1040–1059
- Mavroulis S, Mavrouli M, Carydis P, Agorastos K, Lekkas E (2021) The March 2021 Thessaly Earthquakes and Their Impact Through the Prism of A Multi-Hazard Approach in Disaster Management. *Bull Geol Soc Greece* 58:1–36. <https://doi.org/10.12681/bgsg.26852>
- Michas G, Vallianatos F (2018) Stochastic modeling of nonstationary earthquake time series with long-term clustering effects. *Phys Rev E* 98(4):042107
- Michas G, Vallianatos F (2021) Scaling properties, multifractality and range of correlations in earthquake timeseries: Are earthquakes random? In: Limnios N, Papadimitriou E, Tsaklidis G (eds) *Statistical Methods and Modeling of Seismogenesis*. ISTE Wiley, London
- Michas G, Vallianatos F, Sammonds P (2013) Non-extensivity and long-range correlations in the earthquake activity at the West Corinth rift (Greece). *Nonlinear Process Geophys* 20:713–724
- Michas G (2016) Generalized statistical mechanics description of fault and earthquake populations in Corinth rift (Greece). PhD Thesis, University College London
- Miller SA, Colletini C, Chiaraluce L, Cocco M, Barchi M, Kaus BJ (2004) Aftershocks driven by a high-pressure CO<sub>2</sub> source at depth. *Nature* 427(6976):724–727
- Müller MD, Geiger A, Kahle HG, Veis G, Billiris H, Paradissis D, Felekis S (2013) Velocity and deformation fields in the North Aegean domain, Greece, and implications for fault kinematics, derived from GPS data 1993–2009. *Tectonophysics* 597:34–49
- Nakanishi H (1992) Earthquake dynamics driven by a viscous fluid. *Phys Rev A* 46(8):4689
- Nanjo KZ, Izutsu J, Orihara Y, Kamogawa M, Nagao T (2019) Changes in seismicity pattern due to the 2016 Kumamoto earthquakes identify a highly stressed area on the Hinagu fault zone. *Geophys Res Lett* 46:9489–9496. <https://doi.org/10.1029/2019GL083463>
- Nur A, Booker JR (1972) Aftershocks caused by pore fluid flow? *Science* 175:885–888
- Obana K, Takahashi T, No T, Kaiho Y, Kodaira S, Yamashita M et al (2014) Distribution and migration of aftershocks of the 2010 Mw 7.4 Ogasawara Islands intraplate normal-faulting earthquake related to a fracture zone in the Pacific plate. *Geochem Geophys Geosyst* 15:1363–1373. <https://doi.org/10.1002/2014GC005246>
- Ogata Y (1983) Estimation of the parameters in the modified Omori formula for aftershock frequencies by the maximum likelihood procedure. *J Phys Earth* 31:115–124
- Omi T, Ogata Y, Hirata Y, Aihara K (2013) Forecasting large aftershocks within one day after the main shock. *Sci Rep* 3:2218. <https://doi.org/10.1038/srep02218>
- Omori F (1894) On after-shocks of earthquakes. *J Coll Sci Imp Univ Tokyo* 7:111–200
- Papadimitriou EE, Karakostas VG (2003) Episodic occurrence of strong (Mw≥6.2) earthquakes in Thessalia area (central Greece). *Earth Planet Sci Lett* 215(3–4):395–409
- Papazachos BC, Papazachou CB (2003) *The Earthquakes of Greece*. Ziti Publications, Thessaloniki
- Papazachos BC, Panagiotopoulos DG, Tsapanos TM, Mountrakis DM, Dimopoulos GC (1983) A study of the

- 1980 summer seismic sequence in the Magnesia region of Central Greece. *Geophys J R Astron Soc London* 75:155–168
- Peng Z, Zhao P (2009) Migration of early aftershocks following the 2004 Parkfield earthquake. *Nat Geosci* 2:877–881
- Perfettini H, Avouac JP (2004) Postseismic relaxation driven by brittle creep: a possible mechanism to reconcile geodetic measurements and the decay rate of aftershocks, application to the Chi-Chi earthquake, Taiwan. *J Geophys Res Solid Earth* 109(B2):B02304
- Perfettini H, Avouac JP (2007) Modeling afterslip and aftershocks following the 1992 Landers earthquake. *J Geophys Res* 112:B07409. <https://doi.org/10.1029/2006JB004399>
- Perfettini H, Avouac JP (2014) The seismic cycle in the area of the 2011 Mw9.0 Tohoku-Oki earthquake. *J Geophys Res Solid Earth* 119(5):4469–4515
- Perfettini H, Avouac JP, Tavera H et al (2010) Seismic and aseismic slip on the Central Peru megathrust. *Nature* 465:78–81. <https://doi.org/10.1038/nature09062>
- Perfettini H, Frank WB, Marsan D, Bouchon M (2018) A model of aftershock migration driven by afterslip. *Geophys Res Lett* 45:2283–2293. <https://doi.org/10.1002/2017GL076287>
- Reasenbergh PA, Jones LM (1989) Earthquake hazard after a mainshock in California. *Science* 243(4895):1173–1176. <https://doi.org/10.1126/science.243.4895.1173>
- Savage JC, Svarc JL (1997) Postseismic deformation associated with the 1992 Mw=7.3 Landers earthquake, southern California. *J Geophys Res Solid Earth* 102(B4):7565–7577
- Scholz C (2019) *The Mechanics of Earthquakes and Faulting*, 3rd edn. Cambridge University Press, Cambridge
- Schorlemmer D, Wiemer S, Wyss M (2005) Variations in earthquake-size distribution across different stress regimes. *Nature* 437(7058):539–542
- Shcherbakov R (2021) Statistics and forecasting of aftershocks during the 2019 Ridgecrest, California, earthquake sequence. *J Geophys Res Solid Earth* 126:e2020JB020887. <https://doi.org/10.1029/2020JB020887>
- Shcherbakov R, Turcotte DL (2004) A damage mechanics model for aftershocks. *Pure Appl Geophys* 161(11):2379–2391
- Shcherbakov R, Turcotte DL, Rundle JB (2004) A generalized Omori's law for earthquake aftershock decay. *Geophys Res Lett* 31(11):L11613. <https://doi.org/10.1029/2004GL019808>
- Shcherbakov R, Yakovlev G, Turcotte DL, Rundle JB (2005) Model for the distribution of aftershock interoccurrence times. *Phys Rev Lett* 95. <https://doi.org/10.1103/PhysRevLett.95.218501>
- Shi Y, Bolt BA (1982) The standard error of the magnitude-frequency b-value. *Bull Seismol Soc Am* 87:1074–1077
- Stucchi M, Rovida A, Gomez Capera AA et al (2013) The SHARE European Earthquake Catalogue (SHEEC) 1000–1899. *J Seismol* 17:523–544. <https://doi.org/10.1007/s10950-012-9335-2>
- Tajima F, Kanamori H (1985) Global survey of aftershock area expansion patterns. *Phys Earth Planet Inter* 40:77–134. [https://doi.org/10.1016/0031-9201\(85\)90066-4](https://doi.org/10.1016/0031-9201(85)90066-4)
- Tang C-C, Lin C-H, Peng Z (2014) Spatial-temporal evolution of early aftershocks following the 2010 ML6.4 Jiashian earthquake in southern Taiwan. *Geophys J Int* 199:1772–1783
- Toda S, Stein RS, Reasenbergh PA, Dieterich JH, Yoshida A (1998) Stress transferred by the 1995 Mw= 6.9 Kobe, Japan, shock: effect on aftershocks and future earthquake probabilities. *J Geophys Res Solid Earth* 103(B10):24543–24565
- Toda S, Stein RS, Richards-Dinger K, Bozkurt SB (2005) Forecasting the evolution of seismicity in southern California: animations built on earthquake stress transfer. *J Geophys Res Solid Earth* 110(B5)
- Toda S, Stein RS, Sevilgen V, Lin J (2011) Coulomb 3.3 Graphic-rich deformation and stress-change software for earthquake, tectonic, and volcano research and teaching—user guide. US Geological Survey open-file report 1060: 63
- Tsallis C (2009) *Introduction to nonextensive statistical mechanics: approaching a complex world*. Springer, Berlin
- Utsu T (1966) A statistical significance test of the difference in b-value between two earthquakes groups. *J Phys Earth* 14:37–40
- Utsu T, Ogata Y, Matsu'ura RS (1995) The centenary of the Omori formula for a decay law of aftershock activity. *J Phys Earth* 43:1–33
- Valerio E, Tizzani P, Carminati E, Doglioni C (2017) Longer aftershocks duration in extensional tectonic settings. *Sci Rep* 7(1):1–12
- Vallianatos F, Michas G (2020) Complexity of fracturing in terms of non-extensive statistical physics: from earthquake faults to arctic sea ice fracturing. *Entropy* 22(11):1194
- Vallianatos F, Michas G, Papadakis G, Sammonds P (2012) A non-extensive statistical physics view to the spatiotemporal properties of the June 1995, Aigion earthquake (M6.2) aftershock sequence (West Corinth rift, Greece). *Acta Geophys* 60:758–768
- Vallianatos F, Papadakis G, Michas G (2016) Generalized statistical mechanics approaches to earthquakes and tectonics. *Proc R Soc A* 472(2196):20160497
- Vallianatos F, Pavlou K (2021) Scaling properties of the Mw7.0 Samos (Greece), 2020 aftershock sequence. *Acta Geophys*:1–18. <https://doi.org/10.1007/s11600-021-00579-5>
- Vallianatos F, Michas G, Papadakis G (2018) Nonextensive statistical seismology: an overview. In: *Complexity of seismic time series*, Elsevier, pp 25–59
- Vamvakaris DA, Papazachos CB, Papaioannou CA, Scordilis EM, Karakaisis GF (2016) A detailed seismic zonation model for shallow earthquakes in the broader Aegean area. *Nat Hazard* 16(1):55–84. <https://doi.org/10.5194/nhess-16-55-2016>
- Wells DL, Coppersmith KJ (1994) New empirical relationships among magnitude, rupture length, rupture width,



- rupture area, and surface displacement. *Bull Seismol Soc Am* 84(4):974–1002
- Wessel P, Smith WHF, Scharroo R, Luis J, Wobbe F (2013) Generic Mapping Tools: improved Version Released. *EOS Trans AGU* 94(45):409–410. <https://doi.org/10.1002/2013EO450001>
- Wiemer S, Wyss M (2000) Minimum magnitude of complete reporting in earthquake catalogs: examples from Alaska, the Western United States, and Japan. *Bull Seismol Soc Am* 90:859–869

**Publisher's note** Springer Nature remains neutral with regard to jurisdictional claims in published maps and institutional affiliations.